Chem Soc Rev

Interactions between lasers and two-dimensional transition metal dichalcogenides

SCHOLARONE™
Manuscripts

Chem Soc Rev

Interactions between lasers and two-dimensional transition metal dichalcogenides

Junpeng Lu[a,b], Hongwei Liu*[c], Eng Soon Tok[a] and Chorng-Haur Sow*[a,b]

The recent increasing research interests in two-dimensional (2D) layered materials have led to an explosion of discovery of novel physical and chemical phenomena in these materials. Among the 2D family, group-VI transition metal dichalcogenides (TMDs) represented by MoS_2 and WSe_2 are remarkable semiconductors with sizable energy band gaps. This renders the TMDs promising building blocks of new generation optoelectronics. On the other hand, the specificity and tunability of the band gaps could generate especially strong light-matter interactions between TMDs crystals and specific photons. These interactions can trigger complex and interesting phenomena such as photo-scattering, photo-excitation, photo-destruction, photo-physical modification, photochemical reaction and photo-oxidation. Here, we provide an overview on the phenomena and observations facilitated by various interactions between lasers and 2D TMDs. Characterizations of optical fundamentals of the TMDs *via* laser spectroscopies are reviewed. Subsequently, photoelectric conversion devices enabled by laser excitation and functionality extension and performance improvement of the TMDs materials *via* laser modification are comprehensively summarized in sequence. Finally, we conclude the review with a prospect of the further developments of the research possibilities which could generate from interactions between lasers and TMDs.

1. Introduction

As a forerunner of the 2D material family, graphene has opened up an upsurge in research interests with enticing prospects for future applications since the reduced dimensionality reinvest its novel properties in electronics, optoelectronics and mechanics.[1, 2] However, the gapless feature of pristine graphene lack the capacity to provide the "on/off" switching control for a transistor in the logic circuit. To overcome the short coming of graphene, layered TMDs were revitalized and attracted great attentions in recent research due to their wide variety of chemical compositions and unique properties, especially with the presence of the direct band gap for monolayer.[3] The 2D TMDs, denoted as MX_2, usually possess the repeated unit of X-M-X, where M is the transition metals of Mo, W, Ta, Zr, Re etc., and X is the chalcogens of S, Se and Te. The different filling of d orbitals in these wide ranges of transition metals give rise to MX_2 crystals with versatile properties such as superconducting, metallic, semiconducting and insulating.[4] The big library of TMDs boosts the development of elegant research fields of electronics, photonics, catalysts etc.[5] Among these TMDs, group-VI candidates including MoS_2, $MoSe_2$, WS_2 and WSe_2 attract most of the attentions at the current stage due to their semiconducting behavior and the sizable energy band gaps covering spectral range from visible to near infrared.[6] Similar to graphene, TMDs monolayers can be fabricated through different methods such as mechanical exfoliation,[3] chemical exfoliation[7-9] or chemical vapor deposition (CVD) approaches,[10-13] and can be viewed as the semiconducting counterpart of graphene in the 2D limit. As the focus of the interests at the beginning stage, MoS_2 monolayer was firstly created using the scotch-tape method equipped with the fabrication of graphene.[3] Subsequently, the interesting indirect to direct band gap transition when the MoS_2 is thinned down to monolayer was experimentally observed *via* photoluminescence (PL) spectroscopy.[14, 15] This phenomenon renders the monolayer TMDs as an attractive material for a host of emerging optical and photoelectrical devices. In addition, the reduced screening in two dimensions and the large carrier effective mass facilitated a monolayer field effect transistor (FET) that exhibits superior electron mobility of ~ 200 cm^2 V^{-1} s^{-1} and high on/off ratio.[16] Furthermore, the 2D nature of the materials facilitates high specific surface area. This feature makes TMDs to be extremely sensitive to surface and interface perturbances, *i.e.*, the surface and interface effects can be employed to improve the performance of the electronic devices based on 2D TMDs. As a result, the versatile

[a.] Department of Physics, National University of Singapore, 2 Science Drive 3, Singapore 117542. E-mail: physowch@nus.edu.sg
[b.] Center for Advanced 2D materials and Graphene Research Center, National University of Singapore, 6 Science Drive 2, Singapore 117546.
[c.] Institute of Materials Research and Engineering, A*STAR (Agency for Science, Technology and Research), 2 Fusionopolis Way. Innovis, #08-03, Singapore 138634. E-mail: liuhw@imre.a-star.edu.sg

TMDs monolayers are spectrally robust and amenable to ultimate electrical, optical and photoelectrical devices.

Meanwhile, given the fast increasing demand upon the exploration of 2D TMDs, deep understanding of their fundamental properties, effective implementation of the applications and further expansion of the potentials are particularly desired. Synchronous in the rapid development of the materials with micro/nano scales, various laser-based techniques have been developed to be effective tools to meet different kinds of demands in nanomaterial research. These include nanomaterial characterization,[17, 18] manipulation,[19, 20] activation,[21, 22] modification[23, 24] etc. Interactions between laser and materials could trigger complex and interesting phenomena such as photo-scattering, photo-excitation, photo-destruction, photo-physical modification, photochemical reaction and photo-oxidation. Upon these interactions, laser spectroscopies have been designed to characterize the optical and electrical fundamentals of nanomaterials in an accurate and noninvasive matter;[25] laser light beams are employed to excite and activate optoelectronic devices;[26] laser beams with high powers facilitate the structure manipulation and property modification in a nano-scaled range.[27] Considering the atomic fineness of TMDs monolayers, the handling techniques are required to be straightforward and non-destructive accompanied with high spatial and spectral resolution. Laser technologies satisfy all of the requirements.

Proceed from the fast growing interest in the 2D TMDs research field, this article provides a retrospective review on the interactions between lasers and 2D TMDs with trigonal prismatic phase (2H phase). In this review, we highlight recent advances in the fundamental property characterizations, optoelectronic applications, property modification and improvements of the emerging 2D group-VI TMDs semiconductors, facilitated by laser-based technologies. We first begin with review of the characterizations of optical fundamentals of atomically thin TMDs *via* laser spectroscopies. Subsequently, we summarize the realized photoelectric conversion devices of TMDs enabled by laser excitation. We put an emphasis on the functionality extension and performance improvement of the TMDs materials *via* laser modification. Finally, we conclude the review with an outlook for the challenges and further developments in the research generated from interactions between lasers and TMDs.

2. Fundamental optical property characterizations *via* laser spectroscopies

The fundamental properties of TMDs lattice structure depend on the coordination geometry of the atoms and the electrons in the *d* orbitals. Generally, layered TMDs present different stacking orders and metal coordination geometry, including 1T (trigonal symmetry, one layer per unit cell), 2H (hexagonal symmetry, two layers per unit cell) and 3R (rhombohedral symmetry, three layers per unit cell).[6] 1H is the single layer format of 2H phase with a prismatic unit cell. In such single layer MX_2, each metal atom is fixed in the center of a trigonal

prismatic cage and bounded to six chalcogen atoms *via* primarily covalent intra-layer bonding (Fig. 1a).[28] This structure of monolayer MX_2 facilitates the breaking of the inversion symmetry since there are no matched positions of the chalcogen atoms when the metal atom works as an inversion center[29] (Fig. 1b). Different polytypes of TMDs exhibit different basic properties, for example, the 1T phase MoS_2 was demonstrated to be metallic while 2H phase is semiconducting.[7, 30] Therefore, the present investigations of the optical fundamentals are focused on the 2H phase of TMDs. The metallic nature of 1T phase is caused by the partial filling of the t_{2g} band (d_{xy}, d_{xz}, d_{yz}) and the semiconducting behavior of 2H phase is originated from the complete filling of d_{z^2} with empty d_{xy} and $d_{x^2-y^2}$ orbitals (Fig. 1c, d) as explained by the ligand field theory calculation.[4] Quantitatively identifying optical fundamentals of 2D TMDs could be achieved using laser spectroscopies such as PL and Raman spectroscopy. Further characterizations can be provided by various means of second harmonic generation spectroscopy, transient absorption/reflection (pump-probe) spectroscopy and so on. All these laser spectroscopic studies will be addressed in this review.

2.1 Fundamental optical properties

The optical fundamentals of semiconductors are determined by the electronic band structure. One of the key features of group-VI TMDs is that the electronic band structures exhibits strong dependence on the number of layers.[14] The multilayer
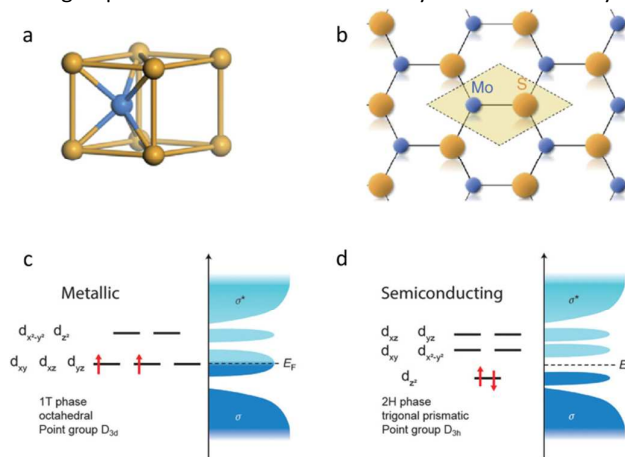

Fig. 1 Schematic of the atomic and electronic structure of TMDs monolayer. (a) Unit cell and (b) top view of the lattice structure. Reproduced with permission from ref. 28. Copyright 2012, Nature Publishing Group. The position of Femi level and Orbital filling of the d-orbitals of (c) 1T and (d) 2H phase. The d-orbitals split into $d_{xy,xz,yz}$ and $d_{x^2-y^2,z^2}$ bands in 1T phase and $d_{xz,yz}$, d_{xy,x^2-y^2} and d_{z^2} in 2H phase. These bands locate at the bonding σ and antibonding σ^* states. Reproduced with permission from ref. 4. Copyright 2013, Nature Publishing Group.
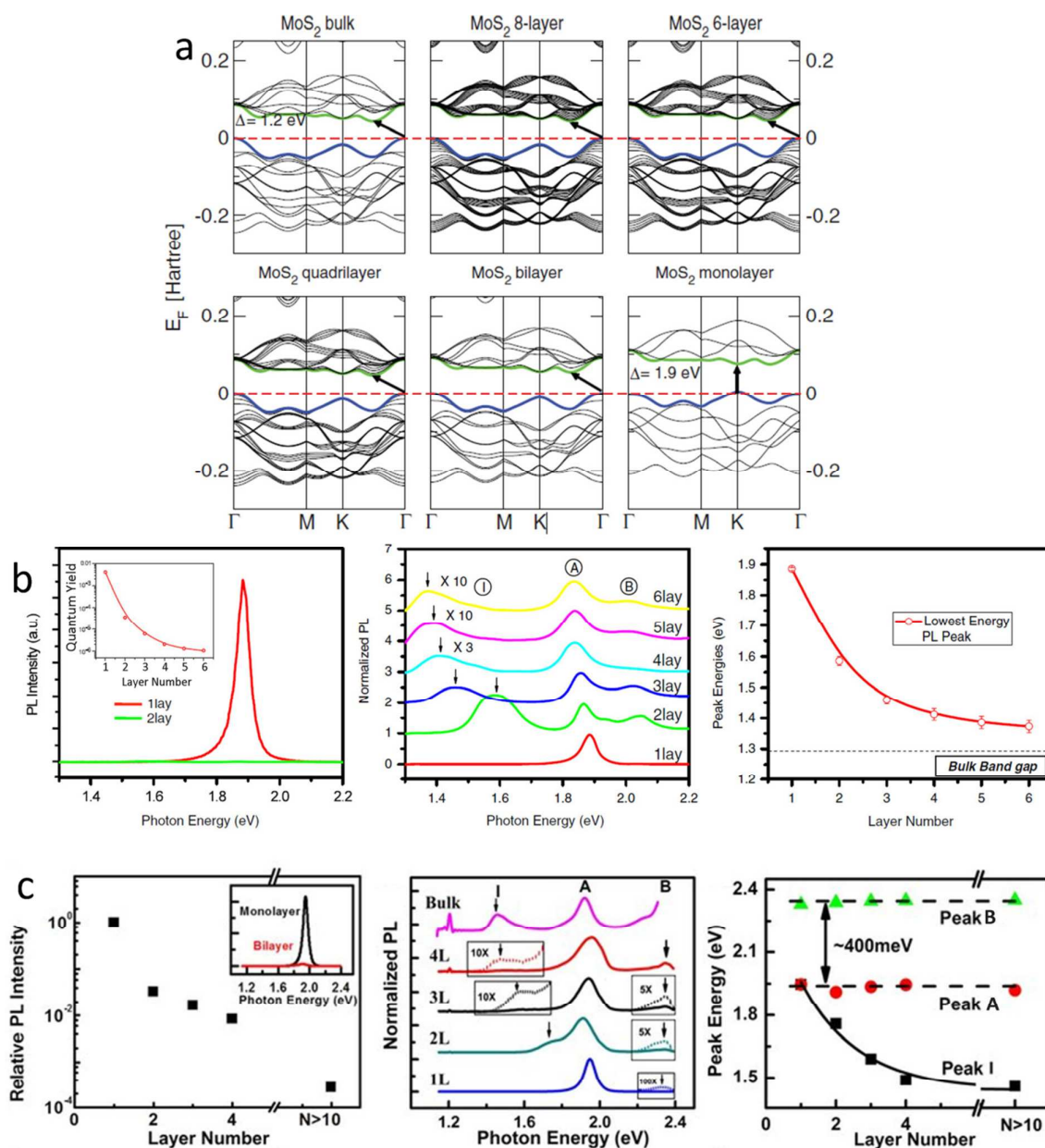
Fig. 2 (a) Calculated band structure of MoS_2 with different layer numbers. Red dash lines indicate the position of Fermi level. Reproduced with permission from ref. 32. Copyright 2011, American Physical Society. Evolution of PL emissions with layer numbers of (b) MoS_2 and (c) WS_2. (b) From left to right, PL spectra of MoS_2 monolayer and bilayer, inset shows the quantum yield as a function of layer numbers; PL spectra of MoS_2 with thickness of 1-6 layers; Band gap energy as a function of layer numbers. Reproduced with permission from ref. 14. Copyright 2010, American Physical Society. (c) From left to right, PL intensity of WS_2 as a function of layer numbers, inset show the PL spectra of monolayer and bilayer; PL spectra of WS_2 with thickness of 1-4 layers and the bulk form; Peak positions of I, A (radiative recombination of A excitons), and B (radiative recombination of B excitons) as a function of layer numbers. Reproduced with permission from ref. 31. Copyright 2013, Nature Publishing Group.

or bulk materials are indirect band gap semiconductors while the band gap of the monolayer counterparts converts to direct band gap at the 2D limit.[14, 15, 31] In multilayers, the indirect band gap is determined by the conduction band minimum (CBM) at the Λ point (Λ_c, midpoint between K and Γ points) and the valence band maximum (VBM) coinciding at the Γ point (Γ_v). When the thickness of the material is thinned down to monolayer, the CBM and VBM shift to and finally coincide at the K point, producing a direct band gap.[33] The electronic states at the Γ point are dominated by the chalcogen P_z
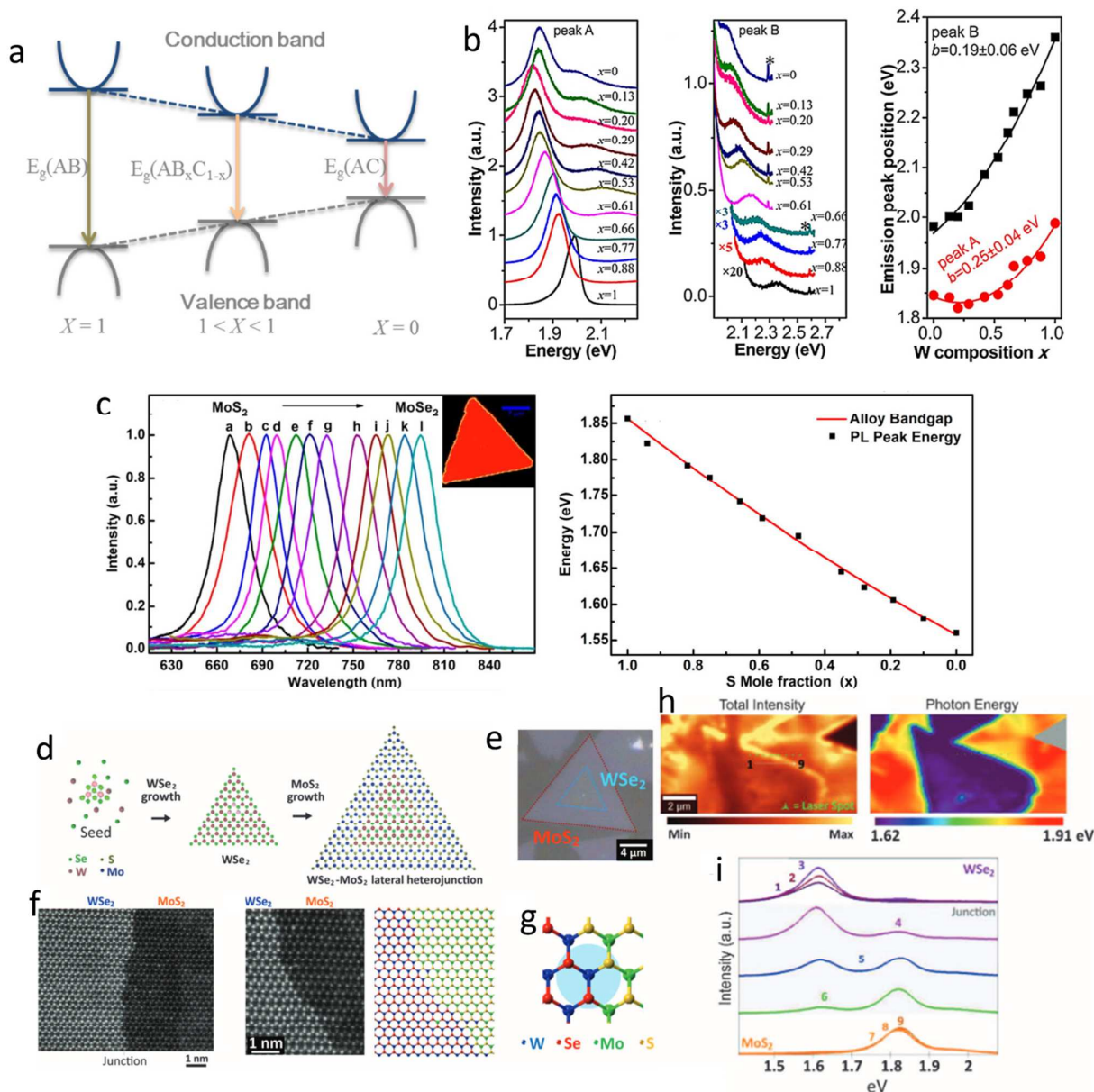
Fig.3 (a) Diagram of the band gaps of ternary alloyed semiconductors. (b) From left to right, A exciton peak at the PL spectra of ternary $Mo_{1-x}W_xS_2$ monolayers; B exciton peak at the PL spectra of ternary $Mo_{1-x}W_xS_2$ monolayers; Peak position of A and B as a function of composition x. Reproduced with permission from ref. 34. Copyright 2013, American Chemical Society. (c) From left to right, PL spectra of $MoS_{2x}Se_{2(1-x)}$ monolayers with different compositions; Peak position as a function of composition x. Reproduced with permission from ref. 35. Copyright 2014, American Chemical Society. (d) Schematic illustration of the growth process, (e) Optical image, (f) TEM images and (g) Atomic model of the WSe_2/MoS_2 monolayer heterojunction. (h) From left to right, PL intensity and peak spatial modulation maps of WSe_2/MoS_2 monolayer heterojunctions. (i) PL spectra collected from nine points as labeled in (h). (d)-(i) Reproduced with permission from ref. 36. Copyright 2015, The American Association for the Advancement of Science.

orbitals which are sensitive to layer number since their charge density extends to the outer surface and is strongly affected by interlayer coupling. Whilst, the electronic states at the K point are mainly determined by the d electrons of the metal atoms. These states are not sensitive to interlayer actions since the metal atoms are confined at the middle of the X-M-X sandwich.[15, 37] Therefore, the evolution of the band gap transition is due to the combined contributions of the quantum confinement effect and interlayer orbital interactions. Fig. 2a shows the calculated electronic band

structure of MoS_2 with monolayer and multilayers using density functional theory (DFT) calculations.[32] The band gap gradually changes from 1.2 eV to 1.9 eV with the thickness thinning down from bulk to monolayer. Simultaneously, the type of the band gap makes a crossover from indirect to direct. The evolution of the transition of the electronic structure and the facilitated optical properties of 2D MX_2 could be monitored by PL spectroscopy *via* collecting the near band edge emissions.[7, 14, 15] The respective PL spectra of MoS_2 and WS_2 with different layer numbers are shown in Fig. 2b, c. The samples are prepared by mechanical exfoliation method. The emission peak-shift (feature I in Fig. 2b, c) clearly demonstrates the broadness of the band gap with thinning of the thickness. Whilst, the quantum yield (PL intensity) provides direct evidence to the transition of the type of the band gap. The much higher (several orders in magnitude) quantum yield in monolayer MX_2 indicates the direct band gap behavior since the involvements of defect- or phonon- scattering which restrict the radiative recombination are suppressed in direct band gap materials.[29] The similar phenomena are also observed from the sample prepared by chemical exfoliation method.[7] This feature renders MX_2 monolayers promising building blocks in various photonics and optoelectronics applications.

In addition, the frequency range of the PL emission could be further extended by chemical or physical methods.[38] Compared to the quantum confinement effect, alloying has been demonstrated to be a convenient technique to engineer the band gap of semiconductors in nanostructure research.[24, 39] Ternary or polynary alloys provide tunable band gaps through controlling their compositions/stoichiometry. For example, the band gap of ternary compound of $AB_xC_{1-x}/A_xB_{1-x}C$ could be continuously tuned from the band gap of AB/AC to band gap of AC/BC with decreasing x. Figure 3a schematically illustrates the tunability of the band gap of AB_xC_{1-x}. Generally, the relationship between the band gaps and the composition x obeys the following quadratic function

$$E_g(x) = E_{AC} + (E_{AB} - E_{AC} - b)x + bx^2 \qquad (1)$$

where E_g and E_{AC}/E_{AB} are the band gaps of the ternary and binary compounds, respectively. b is a bowing parameter describing the miscibility of the ternary alloy. In principle, by alloying of MX_2 to form alloys, the direct band gap of the monolayer alloy could be continuously tuned from 1.55 eV of $MoSe_2$ monolayer to 2.0 eV of WS_2 monolayer, covering the frequency range of visible and near infrared light. The first observation of the tunable direct band gap using PL spectroscopy is realized in ternary $Mo_{1-x}W_xS_2$ monolayers.[34] The ternary alloys are fabricated by mixing the metallic elements. The band gap of the alloy changes from 1.8 eV to 2.0 eV with x increases from 0—1, as revealed by the PL spectra (Fig. 3b). The relatively lower value of the b parameter obtained from the theoretical fitting using Eq. 1 indicates the high miscibility of MoS_2 and WS_2. Compared to the mixing of
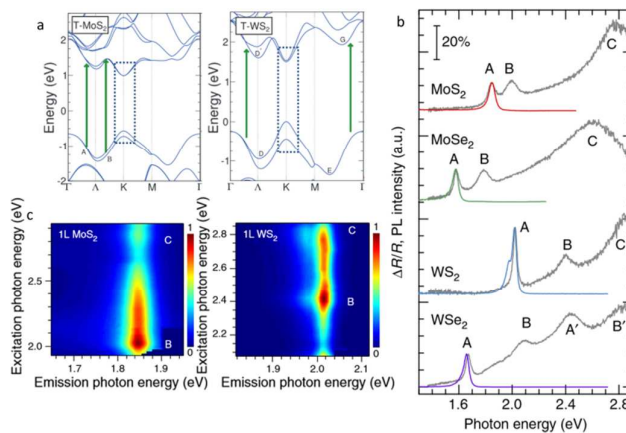

Fig. 4 (a) Calculated band structures of MoS_2 and WS_2 monolayers. The blue dash-lines indicate the splitting of the valence bands. The green arrows indicate the band nesting region. Reproduced with permission from ref. 42. Copyright 2013, American Physical Society. (b) PL spectra (colorized curves) and absorption spectra (gray color curves) of MX_2 monolayers. (c) PL emission intensity maps of MoS_2 and WS_2 monolayers. (b) and (c) Reproduced with permission from ref. 43. Copyright 2014, Nature Publishing Group.

metal elements, more demonstrations of the ternary TMDs monolayers with chalcogen alloying have been reported using CVD methods. By employing a facile one-step CVD method, ternary $MoS_{2x}Se_{2(1-x)}$ monolayers with tunable compositions are synthesized.[35, 40, 41] The direct band gap is measured to gradually vary from 1.87 eV to 1.55 eV as revealed by the PL spectra (Fig. 3c). The relative lower value of b (~ 0.05) obtained from the relationship of band gap energy and the composition factor, x, indicates the high miscibility of the group VI MX_2.

In addition to tune the band gap among distinct samples, band gap engineering within a same monolayer flake is desired to satisfy the rapid development of the high integrated electronics/photonics. To this purpose, in-plane altering of the stoichiometry within a MX_2 monolayer has been designed and realized. The MX_2 monolayer consisting of lateral heterojunction of WS_2/MoS_2,[44] $MoS_2/MoSe_2$,[45] WS_2/WSe_2,[45] $MoSe_2/WSe_2$[46] and WSe_2/MoS_2[36] were synthesized by the modified one-step or two-step CVD methods. Due to the high miscibility of the MX_2, the growth of the heterojunction is epitaxial, realizing the growth of lateral heterojunction to present an atomically sharp and seamless interface (Fig. 3d-i). Take WSe_2/MoS_2 monolayer as an example, the PL spectra exhibit two characteristic peaks corresponding to the band gap of WSe_2 (1.62 eV) and MoS_2 (1.85 eV) (Fig. 3i). PL emission enhancement is found at the heterojunction interface near the WSe_2 part due to the type II band alignment of the junction. Besides the heterojunctions with sharp interface, $MoS_{2(1-x)}Se_{2x}$ monolayer with continuously tunable and laterally graded compositions were synthesized *via* a specially designed CVD approach.[47] Within a single monolayer flake, the composition factor, x, could be continuously engineered from 0 to 0.68

from the center to the edge. Correspondingly, the direct band gap gradually varies from 1.82 eV to 1.64 eV within the single monolayer.

As described by the ligand field theory calculation, the valence and conduction band edges at K points of 2H phase MX$_2$ is determined by the d_{z^2} and d_{xy} / $d_{x^2-y^2}$ orbitals of the heavy metal (Fig. 1d). This distinct d-orbits facilitates significant Zeeman-like spin-orbit coupling in 2D MX$_2$. The calculated band structures of MoS$_2$ and WS$_2$ indicates that the spin-orbit coupling could induce obvious splitting of the valence band at the K points (Fig. 4a).[42] The splitting of the valence band facilitates two interband optical transition paths for the carriers. These two transitions could be monitored by the optical spectra of PL spectra (Fig. 2) and absorption spectra (Fig. 4b), as defined and corresponding to the A and B excitonic transitions. The values of the splitting of group VI MX$_2$ are measured to be ~ 0.15 eV to ~ 0.40 eV according to the spectra,[14, 48, 49] which is slightly smaller than the predicted values of the DFT calculations.[37, 50, 51] The tungsten dichalcogenides present enhanced splitting than molybdenum dichalcogenides due to the heavy mass of tungsten. Besides the information of the spin-orbit splitting, the absorption spectra also exhibits strong absorption peaks at higher energy ranges in MX$_2$ monolayer (Peak C in Fig. 4b). However, this peak is not observed in the PL spectra. As indicated by the calculated band structures (Fig. 4a), the giant absorption is caused by the resonance with the band nesting in the band structures. The band nesting is the region in the band structure where the valence and conduction bands are parallel.[42] The existence of band nesting results in the excitation-dependence of the relaxation paths of the photo-carriers. Since the photoexcited electron and holes possess the same but opposite velocities at the band nesting region, the electron-hole pairs prefer to separate in that space. Therefore, the radiative recombination (PL) is suppressed for absorption in resonance range with band nesting. The excitation-wavelength-dependent relaxation of the photo-carriers could be evaluated by the PL spectra and intensity mapping (Fig. 4c).[43] These unique optical properties establish substantial science bases for the applications of 2D TMDs in photonics and optoelectronics.

2.2 Vibrational properties

Infrared and Raman spectroscopies represent effective techniques to evaluate the low-frequency and high-frequency phonons in solid state physics, respectively. Considering the relatively small size of the TMDs samples, Raman spectroscopy is the most generally used nondestructive and accurate tool to investigate the thickness-dependent lattice vibrations. This is rendered by the high spatial resolution of lasers which are employed as the light sources in Raman spectroscopy. The interlayer interactions of the van der Waals structures facilitate the basic lattice vibrations to present distinct features in layer-number evolution of phonons, interlayer shear, layer breathing phonons etc. Due to the versatility of the Raman spectroscopy, all these phonon-related properties could be clearly elucidated by Raman spectra. In bulk MX$_2$, the lattice vibrations obey the D$_{6h}$ point group symmetry and the corresponding modes at Γ point could be described as $\Gamma = A_{1g} + 2A_{2u} + E_{1g} + 2E_{1u} + 2E_{2g} + E_{2u} + 2B_{2g} + B_{1u}$ where 18 phonon modes are included since the "E" modes are doubly degenerate. Among these modes, A_{1g}, E_{1g} and E_{2g} are Raman active, A_{2u} and one of E_{1u} are IR active, B_{2g}, B_{1u}, and E_{2u} are silent, and A_{2u} and the other E_{1u} are acoustic modes. When the MX$_2$ is thinned down to bilayer, the point group summery is transferred to D$_{3d}$ and the 18 vibrational modes are expressed as $\Gamma = 3A_{1g} + 3A_{2u} + 3E_g + 3E_u$ due to the inversion symmetry, where A_{1g} and E_g are Raman active, others are IR active or acoustic modes. For MX$_2$ monolayer, the symmetry is reduced and belongs to D$_{3h}$. There are only nine phonon modes which can be described as $\Gamma = A_1' + 2A_2'' + 2E' + E''$ where Raman active modes include E' (both Raman and IR active), A_1' and E'' (Fig. 5a).[52] Evidently, A_{1g}, E_{1g} and E_{2g} are Raman active in bulk MX$_2$. By employing the Raman spectroscopy with a back-scattering configuration to monitor the photons of bulk MoS$_2$, three Raman peaks located ~ 33.5 cm^{-1}, 383.6 cm^{-1} and 408.7 cm^{-1} are observed and can be assigned to E_{2g}^2, E_{2g}^1 and A_{1g}, respectively.[53] The E_{1g} is not observed due to its Raman tensor. Intensive research efforts have been done on monitoring the thickness of TMDs via the Raman spectroscopy. As discussed in Fig. 5a, the denotations of the photon modes in bulk and monolayer MX$_2$ are different. When the Raman spectra are used to evaluate the thickness of the material from bulk to monolayer, the high-frequency modes E_{2g}^1 (in-plane vibrational mode) and A_{1g} (out-of-plane mode) are commonly monitored as thickness indicator. The layer number identification is favored by the relative frequency difference between A_{1g} and E_{2g}^1 ($\Delta\omega = A_{1g} - E_{2g}^1$). As demonstrated by Raman spectra of MoS$_2$,[52, 54] E_{2g}^1 presents blue shift while A_{1g} red shifts when the material thinned down from bulk to monolayer (Fig. 5b). For thinner samples (layer number, N < 5), the relationship between $\Delta\omega$ and layer number can be described well by $\Delta\omega = 2.58 - 8.4/N$ (Fig. 5c).[52] However, this description is not suitable for the thickness materials. The shift of the E_{2g}^1 mode with thickness may assign to the long-range Coulombic interactions or structure changes induced by stacking. Whilst, the shift of A_{1g} is caused by the varying restoring forces at different thickness.[54, 55] Similar shift trends of the phonon modes have been also observed in MoSe$_2$,[56] WS$_2$[57] and WSe$_2$.[57] Due to the heavier atomic mass of tungsten, the shifts of the frequencies are less significant.
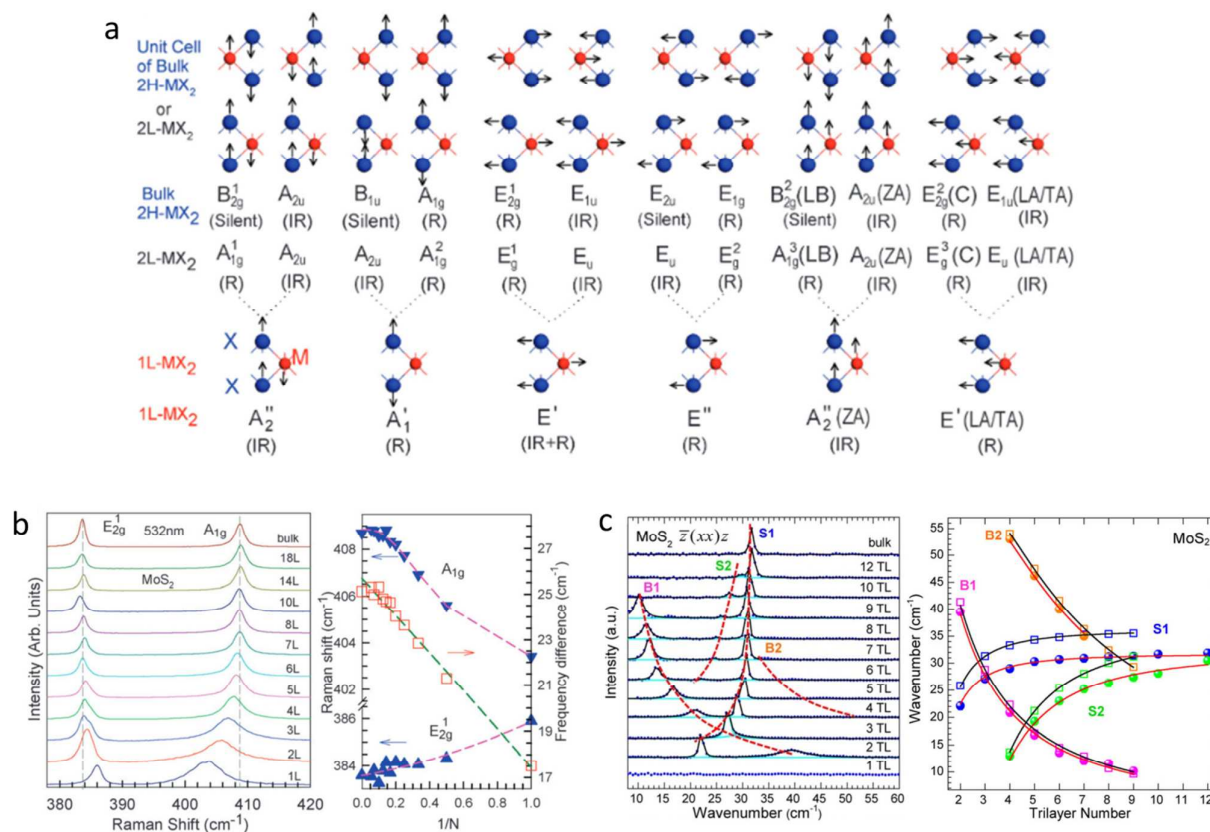
Fig. 5 (a) Schematic of each optical vibration mode for MX$_2$ monolayer, bilayer and bulk. The R, IR and silent stands for Raman-active, infrared-active, and Raman and infrared inactive, respectively. The dash lines indicate that the corresponding in-plate and out-of-plate modes of the bilayer and bulk merge into one in monolayer. (b) From left to right, Raman spectra of MoS$_2$ with different thickness; Frequency of A_{1g}, E_{2g}^2, and the frequency difference of these two modes as a function of 1/N, N means the layer numbers. (a) and (b) Reproduced with permission from ref. 52. Copyright 2015, Royal Society of Chemistry. (c) From left to right, Raman spectra of MoS$_2$ with different thickness at low frequency collected using $\bar{z}(xx)z$ polarization; Frequencies of breathing modes and interlayer shear modes as a function of layer number. Reproduced with permission from ref. 59. Copyright 2013, American Chemical Society.

The determination of the thickness of MX$_2$ by monitoring $\Delta\omega$ is restricted to samples with $N < 5$. The more precise and pertinent approach is to monitor the phonon modes at low frequencies (< 50 cm^{-1}). Take MoS$_2$ as an example, two obvious modes, E_{2g}^2 (interlayer shear mode (C)) and B_{2g}^2 (layer breathing mode (LB)) are observed.[53, 58] These phonon modes originate from the interlayer interactions. As illustrated in Fig. 5a, the C modes are the oscillations of the adjacent layers along the plane direction and the LB modes are the oscillations of the layers perpendicular to the slab. The LB and C modes are absent in MX$_2$ monolayers since there is no interlayer interaction for one layer. Starting from the bilayer, the frequencies of LB modes gradually increase with increasing layer numbers while the frequencies of the C modes present the opposite trend. Several sets of C (defined as S in Fig. 5c) and LB (defined as B in Fig. 5c) modes are observed in MoS$_2$

(Fig. 5c).[59] The LB mode is absent in bulk MoS$_2$ since the LB mode is not Raman active at bulk counterpart. The relationship of the phonon modes at low frequency and the layer numbers can be employed to evaluate the thickness of MoS$_2$ and the applicability is extended to 18 layers.[53] Similar results are also observed in tungsten dichalcogenides.[59]

Considering the high specific surface area, 2D TMDs are predicted to present high sensitivity to external perturbations, such as the changes of environment temperature, infliction of external strains and electrical fields. Given the sensitive vibrational property of the TMDs, Raman spectroscopy is expected to play an important role in probing the external perturbations by carefully analysing the spectra collected under the perturbations. For example, the changes of the temperature can be monitored by observing the peak shifts of E' and A_1' modes of WS$_2$ monolayers. The corresponding Raman spectra of WS$_2$ monolayers at a wide temperature

range (77 - 623 K) have been recorded by Thripuranthaka *et al*.[60] The peak positions of both the E' and A_1' modes shift to lower frequency with increasing temperature. According to the experimental data, the temperature coefficient of the WS$_2$ is extracted to be ~ -0.006 cm^{-1} K^{-1}. In addition to the change of the temperature, the infliction of the external electrical field could also be monitored by the E' and A_1' modes of TMDs monolayers.[61] Applying of gate voltage is a common approach employed to engineer carrier doping to TMDs and tune the output of electronic devices. Simultaneously, the doping of carriers would significantly affect the vibrational property of the TMDs due to the enhanced electron-phonon interactions. Recently, the evolution of E' and A_1' modes of MoS$_2$ monolayers at different applied top-gate voltages has been analysed. The position of the A_1' mode significantly softens while the full wave half maximum of the peak increases with

increasing applied voltages, whereas, the changes of the E' mode are inconspicuous. Since the effect of the gate voltage is to facilitate carrier doping, the shift of the A_1' mode thus can act as readout of the carrier concentration in electronic devices based on TMDS.

2.3 Carrier dynamics

Given the prominent optical properties of 2D TMDs, they are expected to present superior performance in optoelectronics with high efficiencies and fast response. To realize the photoelectrical devices with rapid response rate, it is a prerequisite to understand the ultrafast optical phenomena of the semiconductors at ultrafast time scale. Good performance of TMDs in optoelectronics critically depends on the efficient light absorption and excited carrier relaxation dynamics.
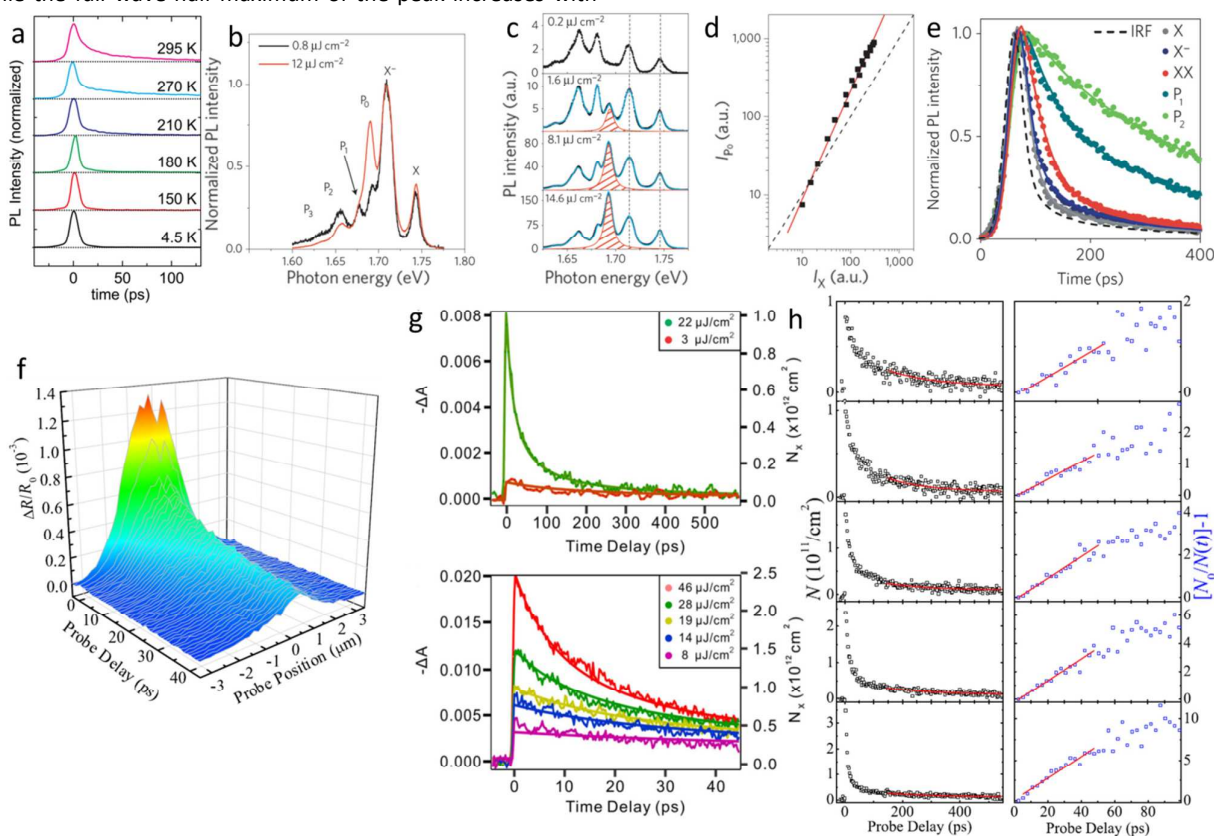

Fig. 6 (a) TRPL spectra of MoS$_2$ monolayers measured at different temperature. Reproduced with permission from ref. 62. Copyright 2011, AIP Publishing LLC. (b) PL spectra of monolayer WSe$_2$ measured at 50 K and excited using fluences of 0.8 and 12 μJ cm^{-2}. (c) PL spectra of monolayer WSe$_2$ at 10 K and excited with different fluences. The identified peaks are same as (b). Only P_o peak changes with fluences. (d) P_o emission strength as a function of exciton emission (*X* peak) strength. (e) TRPL spectra of different peaks labeled in (b). (b)-(e) Reproduced with permission from ref. 63. Copyright 2015, Nature Publishing Group. (f) Differential reflection of WSe$_2$ monolayer as a function of time delay and spatial position. Reproduced with permission from ref. 64. Copyright 2014, American Chemical Society. (g) Differential reflection of MoS$_2$ monolayer pumped using different fluences. The right axis is the density of excitons. The upper and bottom panels show the different time scale ranges. Reproduced with permission from ref. 65. Copyright 2014, American Chemical Society. (h) From left to right, density of excitons as a function of probe delay measured using different fluences (increasing from top to bottom); The quantity $N_o/N(t)-1$ as a function of time delay. *N* is exciton density. Reproduced with permission from ref. 66. Copyright 2014, American Physical Society.
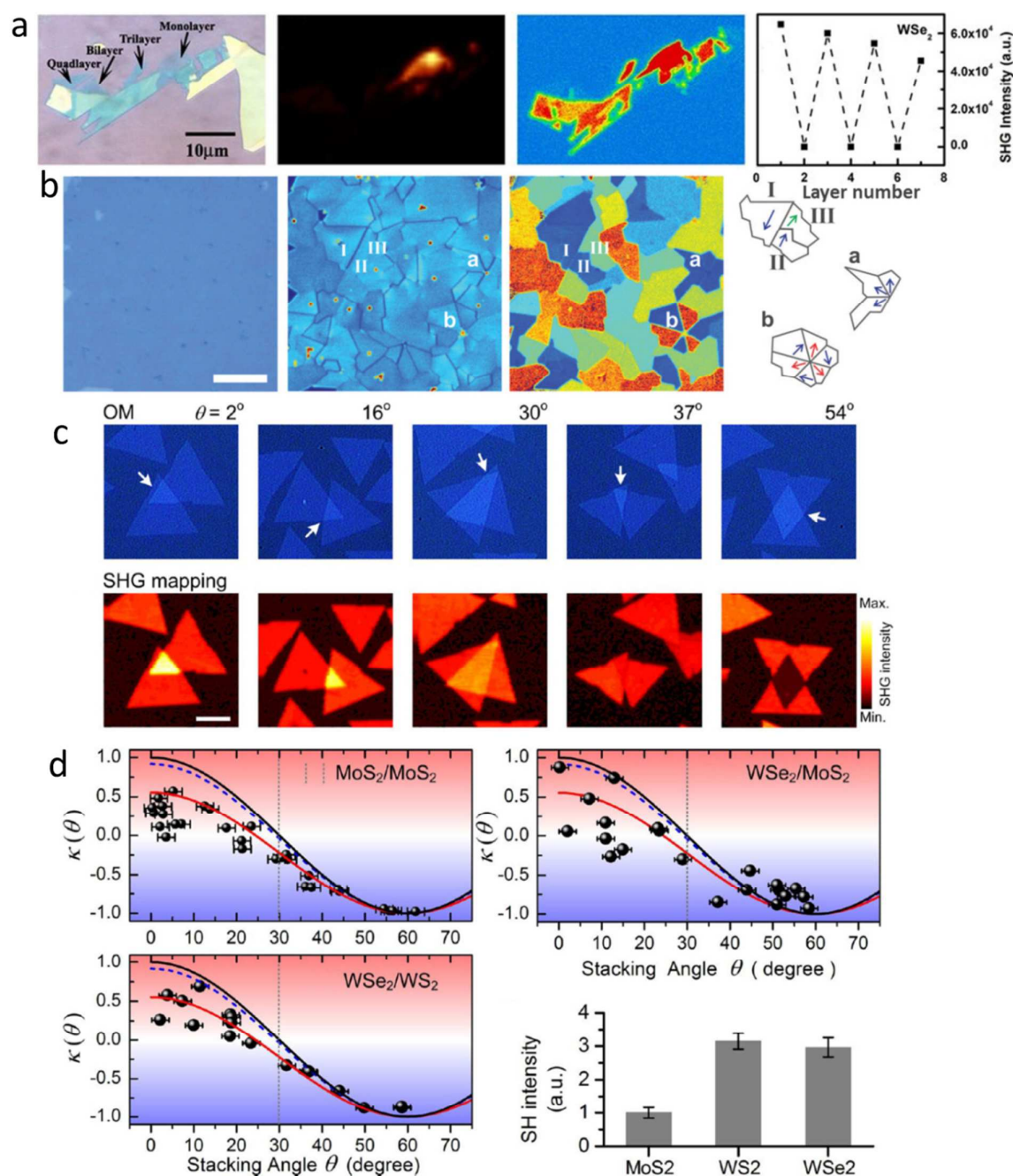
Fig. 7 (a) From left to right, optical image of WS$_2$ flake with domains with different thicknesses; PL map of the same flake; SHG image of the same flake; SHG intensity as a function of layer numbers. Reproduced with permission from ref. 31. Copyright 2013, Nature Publishing Group. (b) From left to right, optical image of CVD-grown monolayer MoS$_2$ film; SHG image of the same film, grains and grain boundaries are clearly shown; Crystal orientation image of the same film, the crystal orientations are clearly identified; Schematics of the crystal orientations of the regions labeled in the images. Reproduced with permission from ref. 67. Copyright 2014, The American Association for the Advancement of Science. (c) Optical images (upper panel) and SHG maps of stacked MoS$_2$ bilayers with different stacking angle. (d) Angular dependence of the quantitative SHG effects ($\kappa(\theta)$) of homo-stacked MoS$_2$/MoS$_2$ and hetero-stacked WSe$_2$/MoS$_2$ and WSe$_2$/WS$_2$ bilayers. $\kappa(\theta)$ is a defined dimensionless parameter as described in Ref 68. The histogram at the bottom right panel shows the SHG intensity of MoS$_2$, WS$_2$ and WSe$_2$ monolayers. (c) and (d) Reproduced with permission from ref. [68]. Copyright 2014, American Chemical Society.

Taking the full advantage of the highly temporal resolution of the ultrafast (femtosecond) pulse laser techniques, ultrafast spectroscopies have been devised to directly monitor the carrier dynamics where the decay time of the carriers in each path (carrier lifetime) could be evaluated while the fundamental mechanisms of the energy loss from the interactions of electron-exciton, exciton-exciton, electron-phonon, *etc.* could be comprehensively determined. The general ultrafast spectroscopies include time-resolved PL (TRPL) spectroscopy and pump probe spectroscopies (*e.g.*, transient absorption/reflection spectroscopies). As described above, since the excitons in monolayer MX2 dominate their optical properties, it is critical to investigate the corresponding excitonic dynamics. Among those ultrafast spectroscopy techniques, TRPL is the most frequently used tool to probe this property. As monitored by the TRPL spectra at different temperature, the PL decay of MoS_2 monolayer is very fast (~ 5 ps) at low temperature while an additional slow recombination process emerges at higher temperature (Fig. 6a).[62] The slow decay process may originate from the exciton-phonon scattering. Besides the classic excitonic behavior as a traditional direct band gap semiconductor, the carriers in 2D TMDs presents strong Coulomb interactions due to the co-existence of the reduced dielectric screening and quantum confinement effects. The strong Coulomb interactions could facilitate tightly bound excitons and additionally lead to higher-order excitonic states such as the observation of charged excitons (trions) and many-body states. Biexciton, a representative four-body state is observed and identified by low temperature PL and TRPL spectroscopies.[63] According to the excitation fluence-dependent analysis, the P_o peak in Fig. 6b presents different trend with other peaks. The intensity of P_o grows superlinearly with increasing excitation densities (Fig. 6c) while the strength of emission from P_o also presents superlinear relationship with respect to exciton emission (*X* in Fig. 6b), as shown in Fig. 6d. Consequently, the P_o peak is identified as the emission from the biexciton (*XX*) states. As further evidence, TRPL spectra are carried out to characterize the dynamics of the biexciton state (Fig. 6e). The life time of biexciton is comparable to those of exciton and trion (*X⁻*). It is around tens of ps. However the lifetime of the emissions from defect related features (P_1 and P_2) is much longer (> 100 ps). Therefore, the emission of P_o is excluded from the defect related states. The binding energy of the biexciton is defined as $\Delta_{XX} = 2E_X - E_{XX}$, where E_X / E_{XX} is the energy of free exciton/biexciton. During the decay process, if the radiative decay of the biexciton is assumed to produce an exciton, the energy of biexciton can be expressed to be $E_{XX} = \hbar\omega_{XX} + E_X = \hbar\omega_{XX} + \hbar\omega_X$, where $\hbar\omega$ is the energy of the radiative emission and can be extracted from the spectra. Therefore, the biexciton binding energy ($\Delta_{XX} = \hbar\omega_X - \hbar\omega_{XX}$) is

calculated to be 52 meV. This value is much higher than those observed in conventional quantum-wells.

Besides the TRPL spectroscopy, transient absorption spectroscopy is another ultrafast technique usually employed to monitor the carrier dynamics in semiconductors. As compared to the TRPL spectroscopy, the characterizations taken by transient absorption spectroscopy would not be effectively affected by the low quantum yield of the materials.[69] In addition to the measurement of carrier lifetime, it is quite straightforward to extract other crucial physical parameters such as mean free path, mobility, diffusion length, exciton diffusion coefficient, *etc*. from analysis of the experimental spectra. By employing this technique on characterization of 2D TMDs system, the lifetime and diffusion coefficient of exciton in WSe_2 monolayer is directly measured.[64] Combining the high resolution of pulse lasers in temporal and spatial domains, the transient absorption spectroscopy could be designed to be an effective approach to investigate the transport property of exciton in WSe_2 monolayer. Fig. 6f depicts such spatiotemporally resolved spectra. This measurement is carried out following a low-density exciton system where the exciton-exciton interaction is not a significant contribution factor to the exciton dynamics. In this case, the exciton transport in WSe_2 monolayer could be described by the classic diffusion equation. Under this description, the exciton diffusion coefficient can be extracted to be $15 \pm 5 \, cm^2$/s *via* theoretically fitting the experimental data. Based on this value, the mean free time, mean free path and mobility are deduced to be 0.24 ps, 17 nm and 600 cm^2/Vs, respectively. Associated with the measured lifetime, the diffusion length is calculated to be 160 nm. All these parameters on exciton dynamics could provide theoretical support to fabrication and optimization of optoelectronics devices based on WSe_2 monolayers. In contrast to the low-density exciton system, the high-density exciton process would exhibit more complex dynamics due to the involvement of exciton-exciton interactions. For instance, another four-body interaction, efficient exciton-exciton annihilation, in MoS_2[65] and $MoSe_2$[66] monolayer have been observed and identified experimentally *via* pump-probe spectroscopy. Exciton-exciton annihilation can be counted as the excitonic analog of Auger recombination. It is a four-body interaction process. During this process, one of the excitons is annihilated and transfers its energy to the other exciton. The dynamics of the MX_2 monolayers present strong dependence on the initial exciton density. Under excitations with high injected density, a fast decay component is observed both in MoS_2 (Fig. 6g) and $MoSe_2$ (Fig. 6h) monolayers. The decay dynamics of the excitons involving the exciton-exciton annihilation process can be theoretically modeled as

$$\frac{dN}{dt} = -k_A N^2 \qquad (2)$$

where N is the exciton density and k_A is the rate of exciton-exciton annihilation. Derived from Equ. 2, the solution is expressed to be

$$N = \frac{N_0}{1 + k_A N_0 t} \qquad (3)$$

where N_0 is the initially photoexcited exciton density. According to these equations, the exciton-exciton annihilation rate of MoS$_2$ and MoSe$_2$ monolayers can be extracted to be $(4.3 \pm 1.1) \times 10^{-2}$ cm^2/s and $(33 \pm 6) \times 10^{-2}$ cm^2/s, respectively, from the experimental spectra. More complicated dynamics process could also be identified by the ultrafast spectroscopy. As described in Section 2.1, the spin-orbit splitting gives rise to two interband transition paths and facilitates two excitons of A and B. Given the affinity of the A and B excitons, a strong A-B interaction is observed in an ultrathin MoS$_2$ film by analysis of the spatiotemporally resolved measurements. The interaction is evaluated by a similar temporal evolution of the transient blue shift and wide broadening of their absorption Gaussians. The identification of these carrier dynamics processes would provide fundamental support to the implementation of 2D TMDs in ultrafast optoelectronics.

2.4 Non-linear optical effects

As discussed in Section 2.2, structure symmetry is a critical factor to engineer the light-matter interactions. The inversion symmetry of monolayer MX$_2$ is broken and reduced to D_{3h} space group. The inversion asymmetry is an underlying reason to facilitate interesting optical properties such as the finite nonlinear optical response in these materials. The optical nonlinearity is important in light-matter interactions. It can facilitate new applications in optoelectronics and photonics where lasers with high intensity are employed. Due to the inversion asymmetry in MX$_2$ monolayers and odd-numbered layers, second order nonlinearity, *i.e.* second harmonic generation (SHG), has been observed in MoS$_2$[70-72], WSe$_2$[31] and WS$_2$[31, 73]. SHG is a typical nonlinear optical process where photons with same frequency interact with a nonlinear material to generate new photons with half wavelength. The observations of SHG in MX$_2$ are identified *via* the laser spectroscopy and imaging techniques. The efficiency of the SHG is quantified by the second-order nonlinear susceptibility
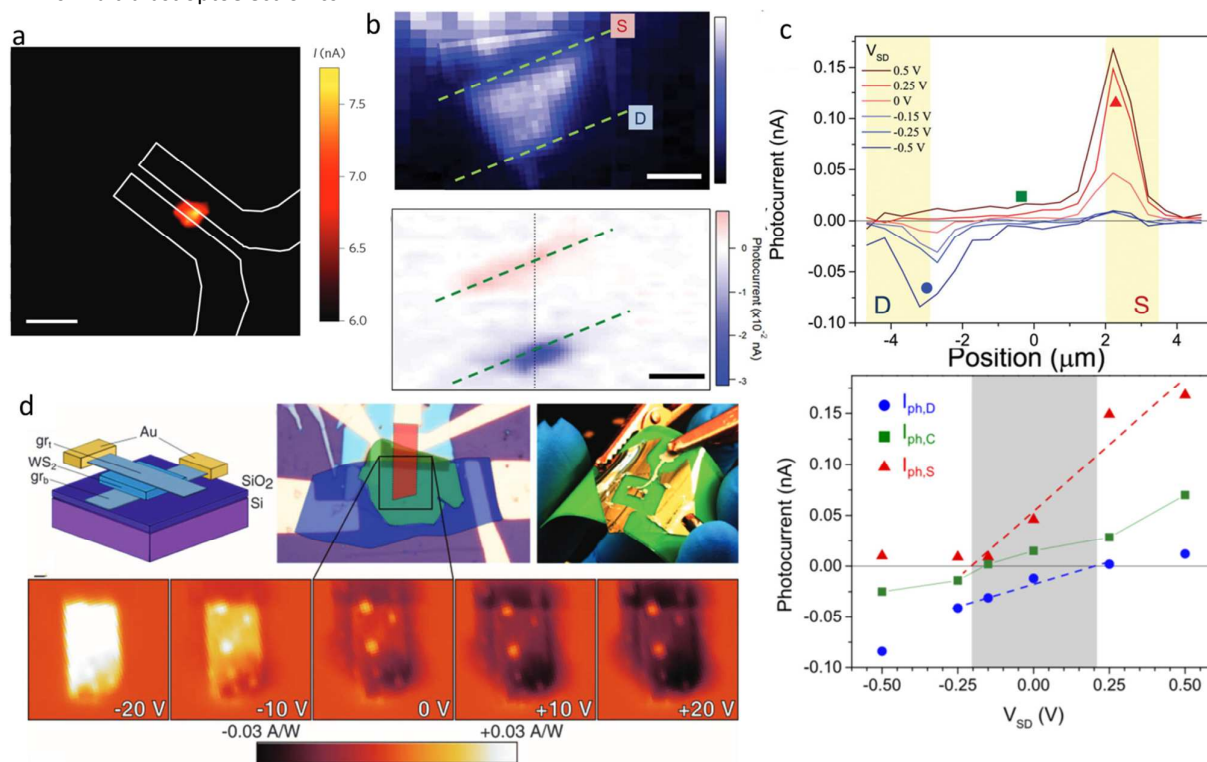

Fig. 8 (a) Photocurrent map of MoS$_2$ monolayer device. Scale bar = 5 μm. Reproduced with permission from ref. 74. Copyright 2013, Nature Publishing Group. (b) PL (upper panel) and photocurrent map of MoS$_2$ monolayer device. Greed dash-lines indicate the positions of the electrodes. (c) Photocurrent line-scan profiles along the device channel at different applied biases (upper panel); Photocurrent amplitude as a function of applied bias measured at the positions labeled in the upper panel. (b) and (c) Reproduced with permission from ref. 75. Copyright 2015, American Chemical Society. (d) Upper panel from left to right: schematic illustration of the stacking device architecture; Optical image of the device; Optical image of a device placed on the flexible substrate. Bottom panel, Photocurrent maps of the stacking device the different applied biases. Reproduced with permission from ref. 76. Copyright 2013, The American Association for the Advancement of Science.

$\chi^{(2)}$. When the inversion symmetry is broken, $\chi^{(2)} \neq 0$. Based on the different efficiencies of SHG from MX$_2$ with different layer numbers, the measurement of SHG can be employed as a sensitive approach to evaluate the thickness of TMDs. Only the samples with odd numbered layers present SHG signal and the intensity of the SHG gradually decreases with increasing thickness (Fig. 7a). In addition to the layer number determination, the SHG imaging can be employed to figure out the crystal grains and grain boundaries, crystal orientations and electronics states variation at the edges of MX$_2$ monolayer (Fig. 7b).[67, 70, 71] The crystal grains and grain boundaries could be directly imaged by the SHG microscopy. The observation of the grain boundaries is enabled by the suppression of SHG at the boundaries. The suppression is arisen from the destructive interference and annihilation of the nonlinear waves from neighboring grains with different orientations. The determination of the crystal orientations is facilitated by the polarization resolved feature of the designed SHG microscopy. The polarization resolved SHG signal is highly dependent on the crystal orientation. The electronic structure variation at the 1D edges is monitored by the enhancement of the SHG intensity at the edges. This SHG technique based on laser spectroscopy demonstrates an easier way in observation of the grains and crystalline orientations in crystals which are thought to be only realized *via* high-resolution electron microscopes. Besides these characterizations, the SHG technique is also demonstrated to determine the stacking orientation of heterostructures consisting of artificial stacking noncentrosymmetric MX$_2$.[68] The SHG of stacked MX$_2$/MX$_2$ twisted bilayers is investigated to be a coherent superposition of the second harmonic fields of each component monolayers. Therefore, it is very sensitive to the stacking angle but insensitive to the component materials. As a result, the SHG technique is efficient to identify the stacking orientation in both homo-stacked and hetero-stacked MX$_2$ bilayers. The evolution has been demonstrated on homo-stacked MoS$_2$/MoS$_2$ and hetero-stacked WSe$_2$/MoS$_2$ and WSe$_2$/WS$_2$ bilayers (Fig. 7c,d).

3. Photoelectric conversion *via* laser excitation

Invariably, the unique optical properties exhibited by the 2D TMDs could be employed to enable photoelectric conversion in optoelectronic devices. Optoelectronic devices can be employed to detect, manipulate, interact with or generate light. Traditional semiconductors have been widely explored as the building blocks in optoelectronics devices such as photodetectors, solar cells, lasers, optical modulators *etc*. Given the special requirements (such as wearable, lighter and transparent) of the next generation optoelectronic devices, flexible and transparent features become essential conditions of the semiconductors. Comparing with the traditional 3D semiconductors, 2D TMDs possess absolute predominance in

such context of optoelectronic devices due to the features of mechanical flexibility, transparency and advantages in fabrication processing. Additionally, the quantum confinement effects in the 2D limit facilitate novel advantages. For instance, the tunable band gap with varying layer numbers leads to the response to photons with different wavelength. Moreover, the high surface to volume ratio of the nano-scaled material provides larger working area for light absorption. Whilst, the surface of the 2D TMDs are naturally dangling bounds free. This leads to the capacity to easily integrate with other components such as cavities and waveguides in optoelectronic systems.

3.1 Photocurrent

The operation of the optoelectronic devices relies on the generation of photocurrent due to photoelectric conversion. The capability of generating photocurrent in 2D TMDs strengthens their potential as building blocks in optoelectronics. With the rapid progress in material synthesis and increasing interests in 2D device fabrication, insight of the photoresponse mechanism and photocurrent origins are important in optimization of the performance of the devices. The origins of the photocurrent in a 2D optoelectronic device are contributed from several factors including light absorption efficiency, photocarrier excitation, free carrier generation, free carrier collection, charge trapping and recombination.[77] Remarkably, the junction at the TMDs-metal electrode interface could also contribute to the photocurrent generation due to the existence of the rectifying Schottky barrier. Therefore, in order to apply 2D TMDs in functional optoelectronic devices, a clear insight into the underlying mechanism of photocurrent generations is desirable. A deep understanding on the mechanism would efficiently guide the device design and optimization. Considering the high spatial resolution of a focused laser beam, the scanning photocurrent microscope (SPCM) can be easily designed to investigate the photocurrent origins.[22, 77] The SPCM has been demonstrated to be well-suited to probe various parameters related to photoresponse in nanostructures, such as carrier diffusion length, electrical field distribution, barrier height and local band bending by monitoring the local photocurrent of the nano-scaled devices.[78-84]

The first time observation of the photocurrent from MX$_2$ monolayer is based on the investigation of the MoS$_2$ monolayer phototransistors.[85] In this early report, a broad laser beam was employed to globally irradiate onto the entire device. In doing so, the contributors to the photoresponse could not be clearly identified and a lower photoresponsivity of 7.5 mA W^{-1} was measured. The lower conductivity and mobility offset the intrinsic advantage of the direct band gap of the MoS$_2$ monolayer and give rise to the lower photoresponsivity. Subsequently, the photodetection device based on MoS$_2$ monolayer was optimized and achieved a 10^5-

fold improvement in the photoresponsivity (880 AW^{-1}).[74] The characterization of the photocurrent is carried out by employing a standard SPCM setup. A microscope objective is used to focus the laser beam. A nanopositioning stage is employed to obtain photocurrent map. The spatially resolved photocurrent distribution could be clearly figured out by scanning the focused laser beam over the device (Fig. 8a). The photocurrent map depicts that the highest photocurrent is generated at the center of the device. This indicates that the MoS$_2$ monolayer is the dominate contributor to the photocurrent generation rather than the junctions of the material and electrodes. On the other hand, the difference of the work functions of the material and metal electrodes would also play an important role in the photocurrent generation. When different metal electrodes are used in a device, the key contribution of the photocurrent would be different. Different from the generation of the photocurrent from the MoS$_2$ monolayer, the highest photocurrent could also be generated at the interface of the MoS$_2$ monolayer/metal electrodes junctions (Fig. 8b).[75] The formation of the current is dominated by the Schottky contacts. By rastering the focused laser beam across the device and, the line profile of the photocurrent could be obtained at a constant bias. After analysis of the profiles at different applied biases, the Schottky barrier height at the MoS$_2$ monolayer/electrode contact can be estimated to be ~ 210 meV (Fig. 8c). In addition, by combining different 2D materials in vertical stacks, heterostructures based on 2D crystals would be formed. These heterostructures represent a new paradigm in optoelectronics. For instance, the heterostructure consisting of graphene/TMDs/graphene is demonstrated to present superior performance in photocurrent generation.[76] The improvement arises from the Van Hove singularities in the density of states of TMDs monolayers. These Van Hove singularities facilitate stronger light absorption and more electron-hole pairs due to the enhanced light-matter interactions. The significant photocurrent generation from the graphene/WS$_2$/graphene stacks is observed and mapped by SPCM measurement (Fig. 8d). Such characterizations carried out by SPCM could unambiguously identify the mechanism of the photocurrent generation. This would clearly guide the design and optimization of the optoelectronic devices based on 2D TMDs.
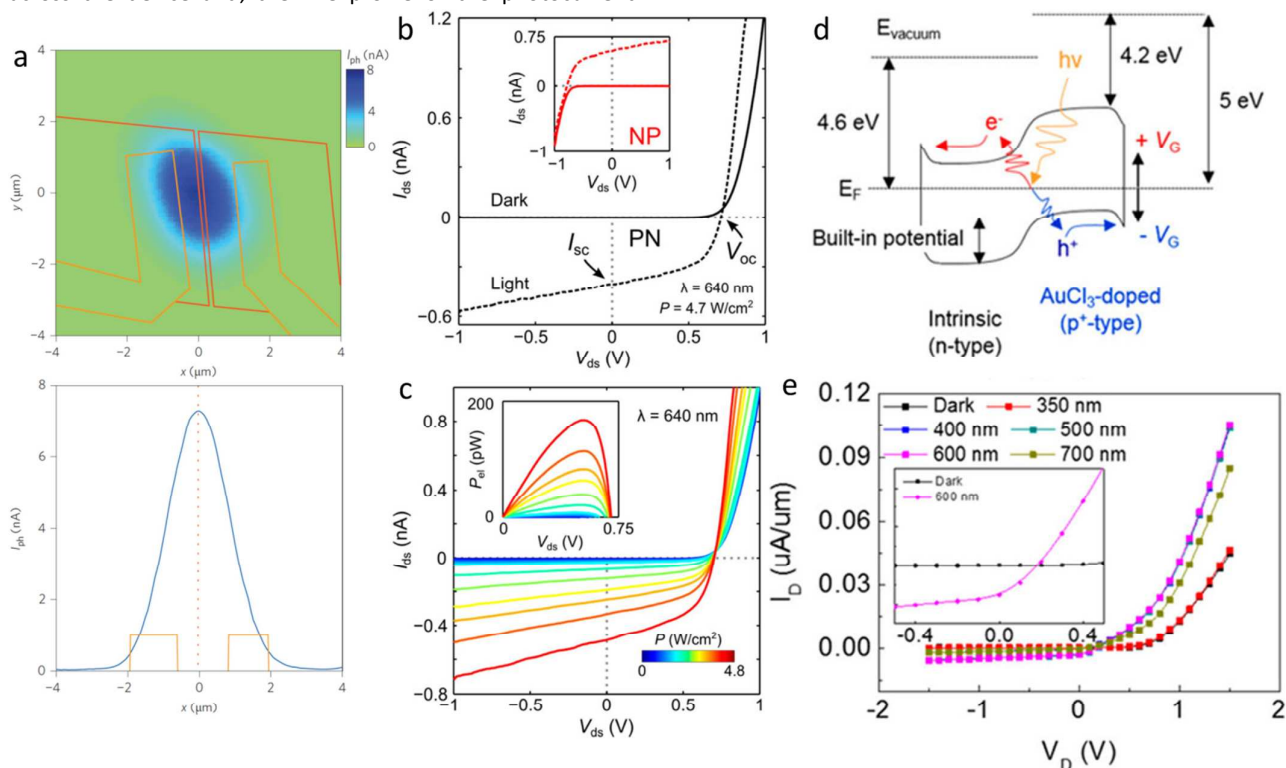

Fig. 9 (a) Photocurrent map and line-scan profile of an electrically tuned p-n junction WSe$_2$ monolayer device measured without bias. Reproduced with permission from ref. 86. Copyright 2014, Nature Publishing Group. (b) I-V curves (with and without laser illumination) of an electrically tuned p-n junction WSe$_2$ monolayer device under the PN configuration. Inset shows the curves under NP configuration. (c) I-V curves of the device under PN configuration with illuminations with different powers. Inset shows the generated power P_{el}, $P_{el} = V_{ds}I_{ds}$. (b) and (c) Reproduced with permission from ref. 87. Copyright 2014, American Chemical Society. (d) Schematic illustration of the band diagram of the p-n junction within MoS$_2$ monolayer. (e) I-V curves of the chemically doping induced p-n junction MoS$_2$ monolayer device under laser illuminations with different powers. (d) and (e) Reproduced with permission from ref. 88. Copyright 2014, American Chemical Society.

3.2 Photovoltaic effect

The photoelectrical conversion based on photovoltaic effect is facilitated by the separation of photoexcited electron-hole pairs by the built-in electric fields. Such electric fields generally locate at the junctions between the regions with different potentials. Among these junctions, p-n junction is one of the most versatile aspects and is considered as foundational component in various optoelectronic devices. Formation of p-n junction requires tightly jointed negatively doped (n-type) and positively doped (p-type) materials. The different doping status in 2D TMDs could be induced by local electrostatic gating[86, 89, 90] or chemical doping.[88] By using the electrostatic gating method, the doping can be flexibly tuned to be n- or p- *via* controlling the applied gate voltages. As an ambipolar semiconductor, p-n junctions could be flexibly configured within WSe$_2$ monolayers *via* electrostatic gating.[86, 89, 90] Upon this electrically controlled p-n junction, significant photocurrent could be generated without applied bias due to the built-in potential. Under the SPCM characterization, the photocurrent is measured when the laser spot scans over the device. The generation of the photocurrent at zero bias is the result of photovoltaic effect and obeys the following process. The electron-hole pairs are excited within WSe$_2$ monolayer by the injected photons. The electron-hole pairs are separated by

the built-in potential at the p-n junction and flow to opposite contacts. The separated carriers are collected by the electrodes to form photocurrent. The photocurrent spatial map and line profile indicate that the maximum photocurrent is measured when the laser is irradiated onto the junction (Fig. 9a).[86] Given the configuration of p-n junction, the presented photovoltaic effect shows promising potential of MX$_2$ monolayers in solar cell applications. Under the laser illumination, the open-circuit voltage (V_{oc}) and short-circuit current (I_{sc}) of the photovoltaic device based on a WSe$_2$ monolayer could be clearly measured (Fig. 9b).[87] With illumination of increasing laser powers, both V$_{oc}$ and I$_{sc}$ increase accordingly and realize higher output electrical power (P$_{el}$, $P = V_{ds}I_{ds}$) (Fig. 9c). Under the illumination using laser with wavelength of 640 nm, the power conversion efficiency of the device is calculated to be ~ 0.01% according to $\eta = P/P_{in}$, where P$_{in}$ is the incident effective power upon the work area. Besides electrostatic gating, chemical doping is another effective approach to facilitate the n- and p-type behavior conversation of MX$_2$. Chemical doping of MoS$_2$ monolayer and multilayers *via* surface modification using Au nanoparticles have been realized to control the properties of the materials in
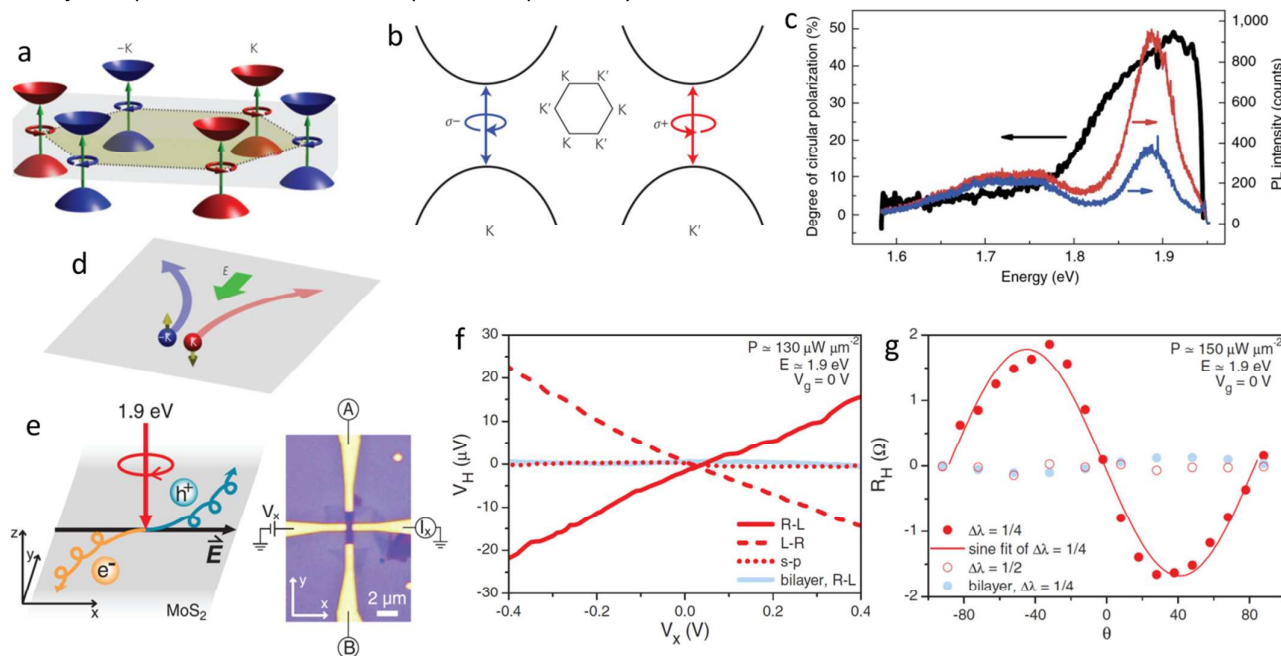

Fig. 10 (a) The schematic diagram of ±K valleys in MX$_2$ monolayer. (b) Schematic of the selection rules at the ±K valleys. Reproduced with permission from ref. 91. Copyright 2012, Nature Publishing Group. (c) PL spectra of MoS$_2$ monolayer excited using circularly polarized laser. The red, blue and black curves corresponds to the σ^+ , σ^- polarizations and the net degree of polarization, respectively. Reproduced with permission from ref. 28. Copyright 2012, Nature Publishing Group. (d) Diagram illustration of the VHE. (a) and (d) Reproduced with permission from ref. 92. Copyright 2014, Nature Publishing Group. (e) Schematic of the photoinduced VHE working principle and optical image of a MoS$_2$ monolayer device. (f) Hall voltage as a function of applied bias. (g) Angle-dependence of the anomalous Hall resistance. (e)-(g) Reproduced with permission from ref. 93. Copyright 2014, The American Association for the Advancement of Science.

optical,[94] electrical[95] and thermoelectrical[96] respects. The occurrence of the surface charge transfer between MoS_2 and $AuCl_4^-$ ions lead to the easy decoration of Au nanoparticles onto MoS_2 surface.[94] During this charge transfer process, Au^{3+} ions attract electrons from MoS_2 and enable significant p-type doping in MoS_2 monolayer or multilayers. Therefore, the lateral p-n junction could be fabricated within a MoS_2 multilayer in such a method *via* converting half of the material from n-type to p-type.[88] The mechanism of the photovoltaic effect induced photoelectrical conversion is schematically illustrated in Fig. 9d. The device based on the p-n junction is demonstrated to present photoresponse to multispectral covering the UV and visible regions (Fig. 9e).

3.3 Valleytronics

The working of traditional electronic devices is based on the movement of electric charge. In addition to electric charge, electronic devices could also be realized by means of other internal degrees of freedom of electrons. Spintronics is a representative example. The working of spintronic devices is facilitated by manipulating the spin angular momentum of electrons. With the observation of graphene, the robust spin states of electrons in the monolayers promote abundant investigations and demonstrations of spintronic devices.[97] Compared to graphene, the hexagonal lattice structures and absence of an inversion center of MX_2 monolayers give rise to additional degree of freedom (DOF) of electrons, valley, upon spin. As described in Section 2.1, the shift of the VBM from Γ point to K points facilitates direct band gaps at the K and −K points in MX_2 monolayers (Fig. 10a).[92] The K and −K valleys are separated by a big momentum space and related to each other by time reversal. This makes them a binary value state system. The manipulation of the DOF of the valleys (K and −K) can be realized by controlling the occupation of them. Since the operations of the manipulation are similar to the spintronics, the concept of "valleytronics" is proposed. Owing to the robust excitons in the ±K valleys, it enables the manipulation of valley DOF by optical approaches.[28, 91, 98, 99] It is predicted that the ±K valleys obey optical selection rules induced by the hexagonal
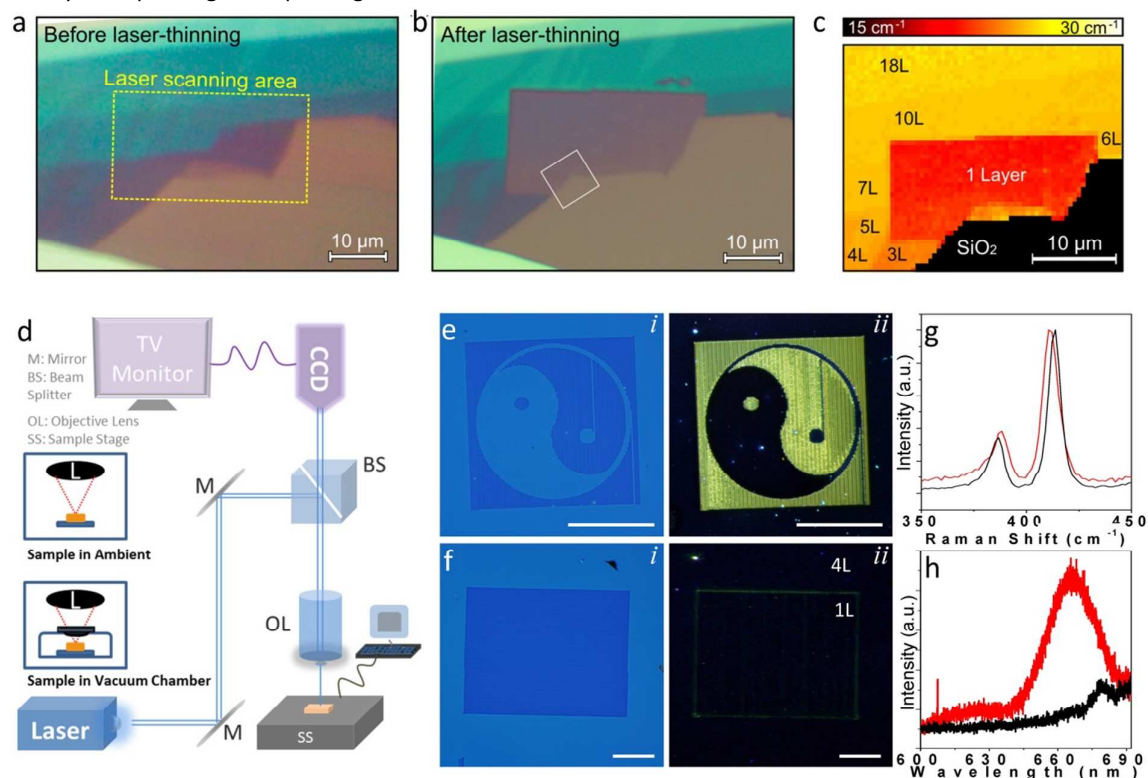

Fig. 11 Optical images of a MoS_2 (a) before and (b) after laser thinning. (c) PL map of the same as shown in (b). The monolayer region created using laser presents higher PL intensity. (a)-(c) Reproduced with permission from ref. 100. Copyright 2012, American Chemical Society. (d) Schematic of a focused laser beam pruning setup. (e) Optical bright field and dark field images of a micropattern created on a MoS_2 film. Scale bar = 20 μm. (f) Optical bright field and dark field images of a monolayer domain fabricated *via* laser thinning within a MoS_2 four-layer film. Scale bar = 20 μm. (g) Raman and (h) PL spectra of the created monolayer (red curves) and pristine regions (black curves) of the MoS_2 film. (d)-(h) Reproduced with permission from ref. 13. Copyright 2014, American Chemical Society.

lattice with inversion asymmetry. The interband transitions at the ±K valleys follow the optical excitations with opposite circular helicity, namely, left/right-hand circularly polarized light (σ_-)/(σ_+) will only excite electrons at the K/−K (defined as K' in Fig. 10b) valley.[91] This selection rules offer a protocol to realize the valley polarization in MX$_2$ monolayers and the exciton valley polarization has been demonstrated in MoS$_2$ monolayers by the polarization-resolved PL (Fig. 10c).[28] The PL results demonstrate the optical circular dichroism, that is, when the monolayers are excited with circularly polarized light, the resulting exciton PL is found to retain the same circular polarization as the excitation light.

The valleytronic devices are aimed to confine electrons to individual momentum valleys as additional DOF in optoelectronic devices. As theoretically predicted, the tight coupling between spin and valley DOF in TMDs would host a combination of valley and Hall effects.[37] Owing to the broken inversion symmetry in TMDs monolayers, there are magnetic moments with equal magnitudes but opposite signs at ±K valleys. Such presented magnetic fields could generate an anomalous velocity to charge carriers excited in the valleys, *i.e.*, the electrons excited from different valleys will undergo Lorentz-like forces with opposite directions and move toward opposite directions perpendicular to the applied bias in the device (Fig. 10d).[92] This phenomenon is called valley Hall effect (VHE). The so-called VHE is demonstrated in a MoS$_2$ monolayer device.[93] Based on a Hall bar device (Fig. 10e), photo-generated anomalous Hall effect could be observed under the excitation of circularly polarized light. The magnitude of the VHE is evaluated by the Hall conductivity σ_H, expressed as

$$\sigma_H \approx -\frac{\hbar \pi \Delta n_v}{2 m_e E_g} \frac{e^2}{h} \tag{4}$$

where m_e is electron band mass, $\hbar = h/2\pi$ where h is Planck's constant, e is elementary charge, n_v is the difference of the photoexcited carrier density between K and −K valleys, and E_g is the band gap of the monolayer. As illustrated in Fig. 10e, under the illumination of circularly polarized light and applied bias along horizontal direction, Hall voltage (V_H) could be obtained along the vertical direction. As a demonstration, anomalous V_H is observed to present linear relation with applied bias under the illumination of light with polarization at the critical point changing from right to left (R-L), whilst, V_H with opposite direction is observed under L-R modulation (Fig. 10f). However, no V_H is observed in MoS$_2$ monolayer under the linear (s-p) polarized light modulation. For MoS$_2$ bilayer, the VHE is not applicable due to the inversion symmetry. The polarization dependence of the VHE in MoS$_2$ monolayer is revealed by the Hall resistance ($R_H = V_H/I_x$) as a function of θ which is the angle between the incident linearly polarized light and the fast axis of the quarter-wave plate (Fig. 10g). Sine relationship is exhibited in the monolayer under circularly

polarized modulation. In addition, the dichroic spin-valley-coupled photogalvanic current is demonstrated in the devices based on MoS$_2$ and WSe$_2$ monolayers,[101, 102] extending the applications of the valleytronics of TMDs monolayers. These demonstrations open up new avenues for photoelectrical conversion in optoelectronics.

4. Functionality extension/improvement via laser modification

Once the materials of TMDs are prepared or synthesized, the range of the potential applications of these materials is restricted by their discrete intrinsic properties. In light of increasing interests to widen the range of applications, it is worthwhile to develop post-treatment techniques. These techniques are desired to have the capacities to improve the properties of the as-synthesized materials and extend their application potentials. Furthermore, to miniaturize functional devices based on TMDs, it is also desirable to develop techniques with the ability to fabricate micropatterns with controlled functionalities on the as-synthesized TMDs. These techniques are required to directly pattern the TMDs as well as alter their properties. Considering the features of high resolution, fast speed and controllable disruption of a scanning
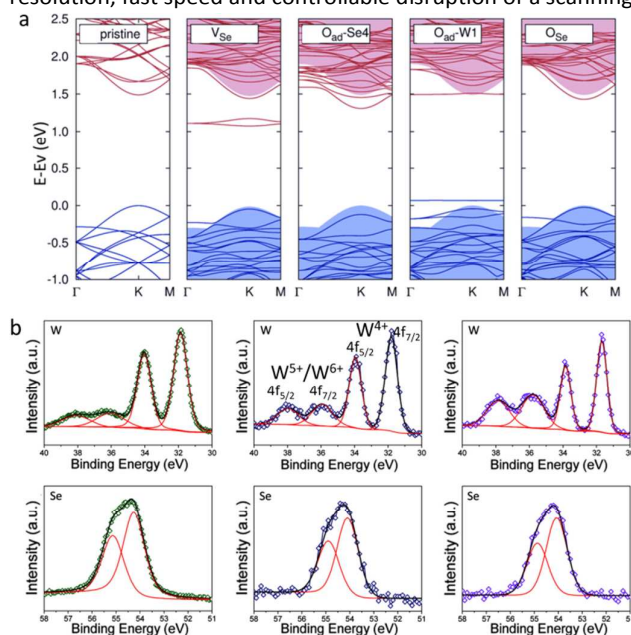
Fig. 12 (a) Calculated band structures of WSe$_2$ monolayer with different defects. From left to right, Pristine; Selenium vacancy; Oxygen adsorbed in the Se4 and W1 configurations; Oxygen substitution of Se. (b) XPS scans of W and Se for pristine WSe$_2$ monolayer; sample modified in environment with lower oxygen concentration; sample modified in environment with higher oxygen concentration (from left to right). (a) and (b) Reproduced with permission from ref. 103. Copyright 2015, American Chemical Society.

focused laser beam, it is rational to develop this technique as a simple, efficient and flexible tool to post-treat the as-synthesized TMDs with the aim to extend and improve their functionalities.

4.1 Direct laser thinning/patterning of TMDs

Considering the increasing demands and wide range of applications shown by the TMDs monolayers, the lower productive rate of the exfoliation approaches is hard to meet the requirement of the fast development. To resolve this issue, considerable efforts have been made to synthesize large area and high quality TMDs monolayers based on different bottom-up strategies. On the other hand, top-down methods based on the postsynthesis procedures have also been developed to further control the thickness of the TMDs. For example, a method based on plasma technique was employed to achieve layer by layer thinning of multilayer MoS_2 to monolayer.[104] To

achieve a better control, techniques based on focused laser beams were designed as a straightforward and effective approach to "on-demand" fabrication of TMDs monolayers. Such a laser thinning method was firstly applied upon mechanically exfoliated MoS_2 multilayers.[100] After scanning the focused laser beam on the multilayered sample with an optimized power density and scanning speed, a uniform monolayer region could be created (Fig. 11a,b). The created monolayer region presents higher PL intensity than the pristine region (Fig. 11c). To extend to the large area MoS_2 films grown by CVD method, the direct thinning and micropatterning could be simultaneously achieved.[13] The as-grown sample is subjected to a focused laser beam setup (Fig. 11d). The sample can absorb the photons and converts the energy to thermal energy. The generated heat facilitates the sublimation of the
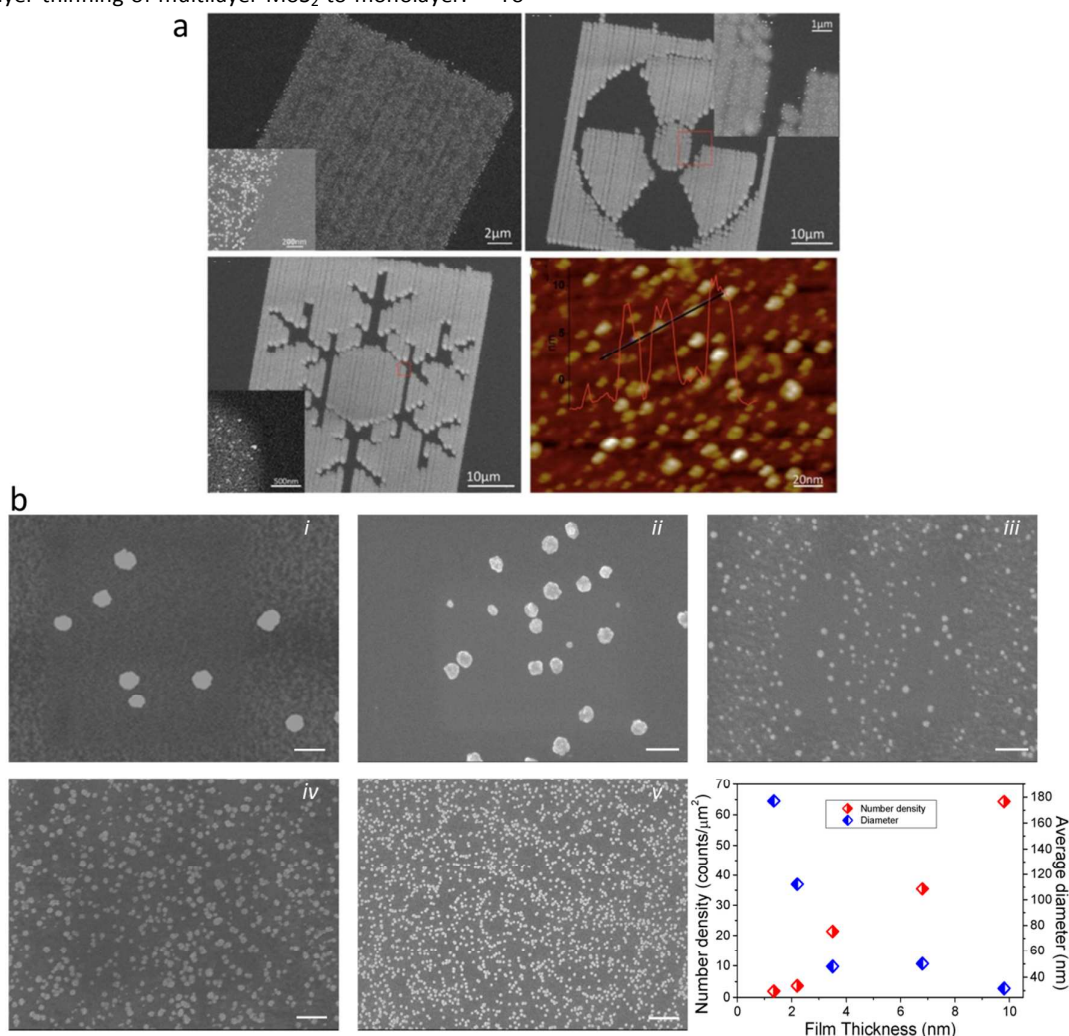

Fig. 13 (a) SEM images of the Au NPs-MoS_2 hybrids. Au NPs only assembled onto the laser modified regions. Bottom right panel is the AFM image of the Au NPs on MoS_2 film. (b) SEM images of the Au nanoparticles on MoS_2 films with different thicknesses. *i–v*: MoS_2 thicknesses are 1.34, 2.2, 3.5, 6.8, and 9.8 nm, respectively. Reproduced with permission from ref. 94. Copyright 2015, John Wiley and Sons.

upper layers to realize the direct thinning. The sample is controlled to move with respect to the laser beam in a programmable manner to achieve the patterning (Fig. 11e). In such a way, versatile functional junctions and components could be fabricated on MoS_2 thin film based on the layer-dependent band gaps. For instance, monolayer domain surrounded by multilayer region can be fabricated (Fig. 11f). The formation of the monolayer domain is identified by the Raman and PL spectra (Fig.11g,h). This "on-demand" method has been demonstrated to be applicable to directly thin and pattern other TMDs (WSe_2[103]) and even other 2D materials such as black phosphorus (phosphorene).[105] Moreover, laser patterning technique could also be employed to fabricate micro-supercapacitors using paintable MoS_2 film.[106] In addition

to the thinning and patterning, this method possesses the capability to modify or alter the property of the samples.

4.2 Photochemical reaction of 2D TMDs

Naturally, the TMDs are chalcogen-deficient due to the higher volatility of the chalcogens.[107] The chalcogen vacancies contribute to the free carrier trapping and scattering. To achieve materials with higher quality, healing the defects with chemical passivation is proposed. Isoelectronic substitutional oxygen defects in TMDs are theoretically demonstrated to be electrically neutral.[103] Therefore, passivation of the chalcogen vacancies using oxygen is a feasible approach to improve the quality of TMDs. The DFT calculations have been carried out on
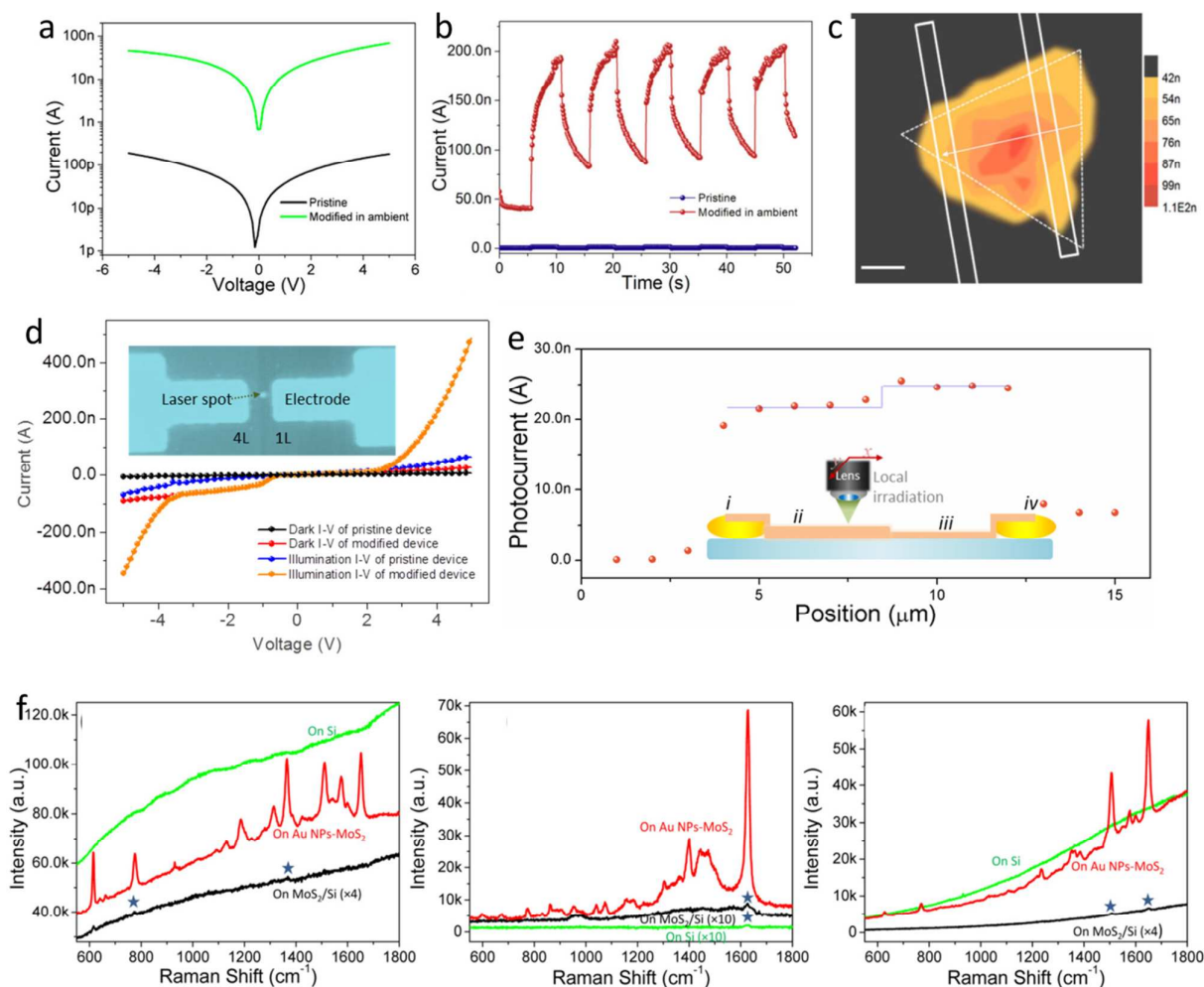

Fig. 14 (a) I-V curves and (b) Photoresponse characteristics of the WSe_2 monolayer device before and after laser modification. (c) Photocurrent map of the device after laser modification. (a)-(c) Reproduced with permission from ref. 103. Copyright 2015, American Chemical Society. (d) I-V curves (with and without laser illumination) of the pristine MoS_2 multilayer device and the device with laser created monolayer-multilayer junction. Inset shows the optical image of the device with laser created junction. (e) Photocurrent profile across the junction measured using SPCM. (d) and (e) Reproduced with permission from ref. 13. Copyright 2014, American Chemical Society. (f) Raman spectra of rhodamine 6G; methylene blue; rhodamine 101 (from left to right), respectively, on Si, MoS_2/Si and Au NPs-MoS_2 substrates. Reproduced with permission from ref. 94. Copyright 2015, John Wiley and Sons.

WSe$_2$ monolayers.[103] The significant unoccupied gap state originating from the Se vacancies could be effectively healed by the oxygen substitution (Fig. 12a). Experimentally, the oxygen substitution has been realized using the focused laser beam technique. The substitution process is controlled by the photochemical reaction between the WSe$_2$ monolayers and oxygen in atmosphere. The degree of the substitution could be controlled by altering the oxygen concentration of the environment. The XPS scans clearly indicate that more oxygen can be introduced into the WSe$_2$ monolayers at the environment with higher oxygen concentration (Fig. 12b). In the W 4f scans, the two doublets are ascribed to W^{4+} in W-Se environment and W^{5+}/W^{6+} in W-O environment, respectively. The oxidization ratio is defined as $I(W^{5+}/W^{6+})/(I(W^{4+})+I(W^{5+}/W^{6+}))$. The ratio gradually increases when the WSe$_2$ monolayers are modified by focused laser beam in environment with higher oxygen concentration. The stoichiometric ratio of W^{4+} and Se could be tailored from ~ 1:1.8 of the pristine sample to be ~ 1:2.0 after the modification of focused laser beam.

Besides the simple photochemical reactions, more complex chemical reactions could be facilitated based on the modification of TMDs using the focused laser beam technique. The 2D configuration of ultrathin TMDs presents a superiorly high surface-to-volume ratio. This feature offers robust surface states since all chemical bonds are exposed upon the surfaces. These surface states make the TMDs extremely sensitive to extraneous perturbations. Therefore, altering the properties of 2D TMDs *via* surface modification would be pronounced and effective. An effective way to enable the surface modification is the decoration of the surfaces with other nano/micro-structures to form functional interfaces. Interfacing with metal nanoparticles (NPs) provides an access to extend the functionality of TMDs. Under the help of a focused laser beam, selective self-assembly of Au NPs on MoS$_2$ has been obtained.[94] The focused laser beam is employed to create micropatterns with active nucleation sites onto the MoS$_2$ surface. Reduction reaction can occur upon the activated surface in AuCl$_3$ solution whereby Au NPs can be selectively assembled onto the modified domains (Fig. 13a). Moreover, the density and size of the Au NPs particles could be easily controlled by tuning the MoS$_2$ thickness (Fig. 13b), reaction time and laser powers. Such a reaction gives rise to localized functionalization of as-grown MoS$_2$ films and creates functional hybrid materials.

4.3 Superior photoelectrical/optical devices

2D TMDs have been successfully demonstrated as good functional materials in various optoelectronic devices. However, the practical applications are constrained by their comparatively low conductivity and photoconductivity. As described in Section 4.2, the lower conductivity of the TMDs is generally due to the trapping or scattering of free carriers induced by chalcogen vacancies. To heal these vacancies, oxygen substitution controlled by a focused laser beam setup has been demonstrated to be a feasible approach. Consequently, the modification *via* the focused laser beam pruning is expected to improve the performance of the optoelectronic devices built on TMDs. Photodetection devices based on WSe$_2$ monolayers have been demonstrated and characterized by different research groups. The photoresponsivity, one of the most important parameter of a photodetector, was measured to be in the range of 0.7-210 mA W^{-1}.[86, 87, 90, 103] Take the standard two-probe device architecture as an example,[103] the photoresponsivity and external quantum efficiency (EQE) of a device based on as-grown WSe$_2$ monolayer are calculated to be 25 mA W^{-1} and 5.8%, respectively, at the medium level of the reported devices. Once the working area (WSe$_2$ monolayer) of the device is globally modified by the focused laser beam, the performance of the device is found to be significantly improved (Fig. 14a-c). The output dark current is measured to be ~ 400-fold higher at the same applied bias than before modification. The corresponding photoresponsivity and EQE are improved to be 3717 mA W^{-1} and 860%, respectively. Therefore, the modification based on the focused laser beam pruning could improve the performance of the optoelectronic devices to be more than two-order higher. Similarly, the enhanced device performance is also achieved on MoS$_2$ transistors after a selectively laser annealing process.[108]

As described in Section 4.1, focused laser beam could be employed as an "on-demand" approach to create functional junctions within MoS$_2$ film. The optoelectronic device built on the monolayer-multilayer junction is demonstrated to present superior performance (Fig. 14d). The difference of the band gaps of the MoS$_2$ monolayer and multilayer enable a significant built-in potential barrier at the junction. The built-in potential would promote the separation of photoexcited electron-hole pairs and generate higher photocurrent. The contributions of the different functional domains are identified by means of SPCM (Fig. 14e). The improvement of the output is ascribed to the synergy of the built-in junction and the introduced defects by laser modification.

Besides the improvement of the optoelectronic devices, the focused laser beam technique could also facilitate optical devices with superior performance. Such a technique has been demonstrated to enable the selectively self-assemble Au NPs onto the surface of MoS$_2$ film to form functional hybrid materials (Fig. 13). Considering the strong coupling of Au NPs to Raman signal and the efficient adsorption of aromatic organic molecules onto MoS$_2$, the obtained Au NPs-MoS$_2$ hybrid is demonstrated as superior surface enhanced Raman scattering (SERS) substrates for the detection of aromatic organic molecules. These SERS substrates present sensitive detection ability to molecules of methylene blue, rhodamine 101 and rhodamine 6G even at the resonance excitation

wavelength (Fig. 14f). With the extensive applicability of the laser techniques, the focused laser beam pruning is expected to play important roles in extending the functionalities of wider 2D materials than TMDs.

5. Conclusions and prospects

In this review, we provide an overview into the use of laser-based technologies as effective tools for the characterization, analysis, modification and manipulation of group-VI 2D TMDs films. Our current understanding on the fundamental optical properties identified *via* various laser spectroscopies is summarized. In particular, the emerging PL is observed by PL spectroscopies, vibrational phonon modes are identified by Raman spectroscopes, dynamics of excitonic carriers are established by various time-resolved spectroscopies, and the non-linear optical behaviors of these TMDs are demonstrated by SHG spectroscopy. Subsequently, the demonstrations of the optoelectronic devices operated by laser excitation are reviewed. Laser excitations could facilitate photoelectric energy conversion within TMDs through different pathways with different mechanism. Finally, the review on the post-synthesis treatments of the TMDs using lasers with subversive energy is presented. The laser beam offers a means to achieve direct thinning and patterning of TMDs for creating monolayer domains. During the fabrication processes, it was also observed that the photoelectrical and optical properties are altered under the effects of induced photochemical reactions. The modified TMDs are demonstrated to present improved functionalities and can be fabricated to be photoelectrical/optical devices with superior performances.

Moving beyond this review, it is worthwhile to believe that the techniques based on lasers has yet to attain their full potential in the research field of 2D TMDs. Although many optical fundamentals have been studied, the understanding of the fundamental properties related to the complex and unique electronic structures of TMDs remain incomplete. For example, the exciton binding energy, one of the key parameters to affect the optical properties, has not been established directly on experiments. Besides the robust exciton-related investigations, more research efforts are also encouraged to focus on the investigation of free carriers rather than excitons because the separated free carriers are the key factor determining the performance of the optoelectronic devices. To this end, laser spectroscopy with frequencies in the terahertz (THz) range might be an effective tool to reach this requirement since THz waves have been demonstrated to be sensitive to free carrier dynamics in semiconductors.[109, 110] On the other hand, higher order many-body interactions in the TMDs monolayers are expected to be observed. The binding energies of the higher order many-body interactions are predicted to be present at higher frequencies. This can extend TMDs roles in optoelectronics with extended response range even to far infrared. Considering the high degree integration of

next generation optoelectronic devices, miniaturize the size of the functional domains and created multifunctional components on a single TMDs sample are desirable. To this end, techniques based on lasers are expected to remain very useful. Given the site selectivity, focused laser beam techniques would be flexible to create functional domains as versatile components on the TMDs. Simultaneously, the laser beams can be employed as the control switches to operate the working of the devices. The high spatial resolution of the focused laser beam facilitates the precisely control of every functional component on the device. Since the components could be individual operated, very complex logic circuits could be achieved. In doing so, more functionalities can be enabled by these devices. In addition, laser technique is an effective tool to construct hybrid nanostructures by combining 2D TMDs with other 0D or 1D nanomaterials. By precisely controlling the architecture of the combination, the hybrids are expected to present superior properties. Based on the designed architecture, the laser beams could also be employed to effectively control the optical and thermal interactions between the beams and the materials to engineer the device performance.

Despite admirable properties have been shown by the typical 2D TMDs, the featured band gaps (1.6 eV - 2.0 eV) of the group-VI MX_2 restrict their light-matter interactions within the visible light range. To pave an avenue for optoelectronic devices working under the control of invisible light (UV or IR), 2D semiconductors with extended band gap ranges would be exploited. As the solid nonmetal monotypic 2D crystal besides graphene, black phosphorus (phosphorene) has been demonstrated to present encouraging properties. The direct band gap of the material can be flexibly tuned from 0.3 eV to 2.0 eV with the thickness reducing from bulk to monolayer.[111, 112] This facilitates considerable light matter interactions in the visible and IR light ranges. In addition, the focused laser modification technique could realize *in situ* oxidization of the phosphorene to form phosphorene oxides. By controlling the oxygen concentration, the band gap of the material can be extended from 2.3 eV to 5.0 eV.[105] This makes the photoresponse of the material covering the spectrum range from UV to IR. Besides phosphorene, arsenene and antimonene has been theoretically predicted to present the indirect band gaps of 2.5 eV and 2.3 eV, respectively. This also extends the photoresponse of the materials to shorter wavelength range.[113]

Acknowledgements

Notes and references

1   K. S. Novoselov, A. K. Geim, S. V. Morozov, D. Jiang, M. I. Katsnelson, I. V. Grigorieva, S. V. Dubonos and A. A. Firsov, *Nature*, 2005, **438**, 197-200.

2   A. H. Castro Neto, F. Guinea, N. M. R. Peres, K. S. Novoselov and A. K. Geim, *Reviews of Modern Physics*, 2009, **81**, 109-162.

3   K. S. Novoselov, D. Jiang, F. Schedin, T. J. Booth, V. V. Khotkevich, S. V. Morozov and A. K. Geim, *Proceedings of the National Academy of Sciences of the United States of America*, 2005, **102**, 10451-10453.

4   M. Chhowalla, H. S. Shin, G. Eda, L.-J. Li, K. P. Loh and H. Zhang, *Nat Chem*, 2013, **5**, 263-275.

5   Y. Sun, S. Gao, F. Lei and Y. Xie, *Chemical Society Reviews*, 2015, **44**, 623-636.

6   Q. H. Wang, K. Kalantar-Zadeh, A. Kis, J. N. Coleman and M. S. Strano, *Nat Nano*, 2012, **7**, 699-712.

7   G. Eda, H. Yamaguchi, D. Voiry, T. Fujita, M. Chen and M. Chhowalla, *Nano Letters*, 2011, **11**, 5111-5116.

8   J. N. Coleman, M. Lotya, A. O'Neill, S. D. Bergin, P. J. King, U. Khan, K. Young, A. Gaucher, S. De, R. J. Smith, I. V. Shvets, S. K. Arora, G. Stanton, H.-Y. Kim, K. Lee, G. T. Kim, G. S. Duesberg, T. Hallam, J. J. Boland, J. J. Wang, J. F. Donegan, J. C. Grunlan, G. Moriarty, A. Shmeliov, R. J. Nicholls, J. M. Perkins, E. M. Grieveson, K. Theuwissen, D. W. McComb, P. D. Nellist and V. Nicolosi, *Science*, 2011, **331**, 568-571.

9   Z. Zeng, Z. Yin, X. Huang, H. Li, Q. He, G. Lu, F. Boey and H. Zhang, *Angewandte Chemie International Edition*, 2011, **50**, 11093-11097.

10   Y.-H. Lee, X.-Q. Zhang, W. Zhang, M.-T. Chang, C.-T. Lin, K.-D. Chang, Y.-C. Yu, J. T.-W. Wang, C.-S. Chang, L.-J. Li and T.-W. Lin, *Advanced Materials*, 2012, **24**, 2320-2325.

11   Y. Zhan, Z. Liu, S. Najmaei, P. M. Ajayan and J. Lou, *Small*, 2012, **8**, 966-971.

12   K.-K. Liu, W. Zhang, Y.-H. Lee, Y.-C. Lin, M.-T. Chang, C.-Y. Su, C.-S. Chang, H. Li, Y. Shi, H. Zhang, C.-S. Lai and L.-J. Li, *Nano Letters*, 2012, **12**, 1538-1544.

13   J. Lu, J. H. Lu, H. Liu, B. Liu, K. X. Chan, J. Lin, W. Chen, K. P. Loh and C. H. Sow, *ACS Nano*, 2014, **8**, 6334-6343.

14   K. F. Mak, C. Lee, J. Hone, J. Shan and T. F. Heinz, *Physical Review Letters*, 2010, **105**, 136805.

15   A. Splendiani, L. Sun, Y. Zhang, T. Li, J. Kim, C.-Y. Chim, G. Galli and F. Wang, *Nano Letters*, 2010, **10**, 1271-1275.

16   RadisavljevicB, RadenovicA, BrivioJ, GiacomettiV and KisA, *Nat Nano*, 2011, **6**, 147-150.

17   G. Gouadec and P. Colomban, *Progress in Crystal Growth and Characterization of Materials*, 2007, **53**, 1-56.

18   C.-H. Chuang and C. Burda, *The Journal of Physical Chemistry Letters*, 2012, **3**, 1921-1927.

19   B. J. Y. Tan, C. H. Sow, K. Y. Lim, F. C. Cheong, G. L. Chong, A. T. S. Wee and C. K. Ong, *The Journal of Physical Chemistry B*, 2004, **108**, 18575-18579.

20   K. Y. Lim, C. H. Sow, J. Lin, F. C. Cheong, Z. X. Shen, J. T. L. Thong, K. C. Chin and A. T. S. Wee, *Advanced Materials*, 2003, **15**, 300-303.

21   Z. H. Lim and C.-H. Sow, *Advanced Functional Materials*, 2010, **20**, 847-852.

22   J. Lu, H. Liu, S. Deng, M. Zheng, Y. Wang, J. A. van Kan, S. H. Tang, X. Zhang, C. H. Sow and S. G. Mhaisalkar, *Nanoscale*, 2014, **6**, 7619-7627.

23   X. Lim, H. W. G. Foo, G. H. Chia and C.-H. Sow, *ACS Nano*, 2010, **4**, 1067-1075.

24   J. Lu, X. Lim, M. Zheng, S. G. Mhaisalkar and C.-H. Sow, *ACS Nano*, 2012, **6**, 8298-8307.

25   J. Cabanillas-Gonzalez, G. Grancini and G. Lanzani, *Advanced Materials*, 2011, **23**, 5468-5485.

26   F. H. L. Koppens, T. Mueller, P. Avouris, A. C. Ferrari, M. S. Vitiello and M. Polini, *Nat Nano*, 2014, **9**, 780-793.

27   O. M. Marago, P. H. Jones, P. G. Gucciardi, G. Volpe and A. C. Ferrari, *Nat Nano*, 2013, **8**, 807-819.

28   T. Cao, G. Wang, W. Han, H. Ye, C. Zhu, J. Shi, Q. Niu, P. Tan, E. Wang, B. Liu and J. Feng, *Nat Commun*, 2012, **3**, 887.

29   H. Zeng and X. Cui, *Chemical Society Reviews*, 2015, **44**, 2629-2642.

30   S. N. Shirodkar and U. V. Waghmare, *Physical Review Letters*, 2014, **112**, 157601.

31   H. Zeng, G.-B. Liu, J. Dai, Y. Yan, B. Zhu, R. He, L. Xie, S. Xu, X. Chen, W. Yao and X. Cui, *Scientific Reports*, 2013, **3**, 1608.

32   A. Kuc, N. Zibouche and T. Heine, *Physical Review B*, 2011, **83**, 245213.

33   H. Schmidt, F. Giustiniano and G. Eda, *Chemical Society Reviews*, 2015.

34   Y. Chen, J. Xi, D. O. Dumcenco, Z. Liu, K. Suenaga, D. Wang, Z. Shuai, Y.-S. Huang and L. Xie, *ACS Nano*, 2013, **7**, 4610-4616.

35   H. Li, X. Duan, X. Wu, X. Zhuang, H. Zhou, Q. Zhang, X. Zhu, W. Hu, P. Ren, P. Guo, L. Ma, X. Fan, X. Wang, J. Xu, A. Pan and X. Duan, *Journal of the American Chemical Society*, 2014, **136**, 3756-3759.

36   M.-Y. Li, Y. Shi, C.-C. Cheng, L.-S. Lu, Y.-C. Lin, H.-L. Tang, M.-L. Tsai, C.-W. Chu, K.-H. Wei, J.-H. He, W.-H. Chang, K. Suenaga and L.-J. Li, *Science*, 2015, **349**, 524-528.

37   D. Xiao, G.-B. Liu, W. Feng, X. Xu and W. Yao, *Physical Review Letters*, 2012, **108**, 196802.

38   H. Wang, H. Yuan, S. Sae Hong, Y. Li and Y. Cui, *Chemical Society Reviews*, 2015, **44**, 2664-2680.

39   L. Junpeng, S. Cheng, Z. Minrui, N. Mathews, L. Hongwei, C. Gin Seng, Z. Xinhai, S. G. Mhaisalkar and S. Chorng Haur, *The Journal of Physical Chemistry C*, 2011, **115**, 19538-19545.

40   Q. Feng, Y. Zhu, J. Hong, M. Zhang, W. Duan, N. Mao, J. Wu, H. Xu, F. Dong, F. Lin, C. Jin, C. Wang, J. Zhang and L. Xie, *Advanced Materials*, 2014, **26**, 2648-2653.

41   Y. Gong, Z. Liu, A. R. Lupini, G. Shi, J. Lin, S. Najmaei, Z. Lin, A. L. Elías, A. Berkdemir, G. You, H. Terrones, M. Terrones, R. Vajtai, S. T. Pantelides, S. J. Pennycook, J.

Lou, W. Zhou and P. M. Ajayan, *Nano Letters*, 2014, **14**, 442-449.

42 A. Carvalho, R. M. Ribeiro and A. H. Castro Neto, *Physical Review B*, 2013, **88**, 115205.

43 D. Kozawa, R. Kumar, A. Carvalho, K. Kumar Amara, W. Zhao, S. Wang, M. Toh, R. M. Ribeiro, A. H. Castro Neto, K. Matsuda and G. Eda, *Nat Commun*, 2014, **5**.

44 Y. Gong, J. Lin, X. Wang, G. Shi, S. Lei, Z. Lin, X. Zou, G. Ye, R. Vajtai, B. I. Yakobson, H. Terrones, M. Terrones, Beng K. Tay, J. Lou, S. T. Pantelides, Z. Liu, W. Zhou and P. M. Ajayan, *Nat Mater*, 2014, **13**, 1135-1142.

45 X. Duan, C. Wang, J. C. Shaw, R. Cheng, Y. Chen, H. Li, X. Wu, Y. Tang, Q. Zhang, A. Pan, J. Jiang, R. Yu, Y. Huang and X. Duan, *Nat Nano*, 2014, **9**, 1024-1030.

46 C. Huang, S. Wu, A. M. Sanchez, J. J. P. Peters, R. Beanland, J. S. Ross, P. Rivera, W. Yao, D. H. Cobden and X. Xu, *Nat Mater*, 2014, **13**, 1096-1101.

47 H. Li, Q. Zhang, X. Duan, X. Wu, X. Fan, X. Zhu, X. Zhuang, W. Hu, H. Zhou, A. Pan and X. Duan, *Journal of the American Chemical Society*, 2015, **137**, 5284-5287.

48 J. A. Schuller, S. Karaveli, T. Schiros, K. He, S. Yang, I. Kymissis, J. Shan and R. Zia, *Nat Nano*, 2013, **8**, 271-276.

49 W. Zhao, R. M. Ribeiro, M. Toh, A. Carvalho, C. Kloc, A. H. Castro Neto and G. Eda, *Nano Letters*, 2013, **13**, 5627-5634.

50 J. S. Ross, S. Wu, H. Yu, N. J. Ghimire, A. M. Jones, G. Aivazian, J. Yan, D. G. Mandrus, D. Xiao, W. Yao and X. Xu, *Nat Commun*, 2013, **4**, 1474.

51 Z. Y. Zhu, Y. C. Cheng and U. Schwingenschlögl, *Physical Review B*, 2011, **84**, 153402.

52 X. Zhang, X.-F. Qiao, W. Shi, J.-B. Wu, D.-S. Jiang and P.-H. Tan, *Chemical Society Reviews*, 2015, **44**, 2757-2785.

53 X. Zhang, W. P. Han, J. B. Wu, S. Milana, Y. Lu, Q. Q. Li, A. C. Ferrari and P. H. Tan, *Physical Review B*, 2013, **87**, 115413.

54 C. Lee, H. Yan, L. E. Brus, T. F. Heinz, J. Hone and S. Ryu, *ACS Nano*, 2010, **4**, 2695-2700.

55 H. Li, Q. Zhang, C. C. R. Yap, B. K. Tay, T. H. T. Edwin, A. Olivier and D. Baillargeat, *Advanced Functional Materials*, 2012, **22**, 1385-1390.

56 P. Tonndorf, R. Schmidt, P. Böttger, X. Zhang, J. Börner, A. Liebig, M. Albrecht, C. Kloc, O. Gordan, D. R. T. Zahn, S. Michaelis de Vasconcellos and R. Bratschitsch, *Opt. Express*, 2013, **21**, 4908-4916.

57 W. Zhao, Z. Ghorannevis, K. K. Amara, J. R. Pang, M. Toh, X. Zhang, C. Kloc, P. H. Tan and G. Eda, *Nanoscale*, 2013, **5**, 9677-9683.

58 H. Zeng, B. Zhu, K. Liu, J. Fan, X. Cui and Q. M. Zhang, *Physical Review B*, 2012, **86**, 241301.

59 Y. Zhao, X. Luo, H. Li, J. Zhang, P. T. Araujo, C. K. Gan, J. Wu, H. Zhang, S. Y. Quek, M. S. Dresselhaus and Q. Xiong, *Nano Letters*, 2013, **13**, 1007-1015.

60 T. M and D. J. Late, *ACS Applied Materials & Interfaces*, 2014, **6**, 1158-1163.

61 B. Chakraborty, A. Bera, D. V. S. Muthu, S. Bhowmick, U. V. Waghmare and A. K. Sood, *Physical Review B*, 2012, **85**, 161403.

62 T. Korn, S. Heydrich, M. Hirmer, J. Schmutzler and C. Schüller, *Applied Physics Letters*, 2011, **99**, 102109.

63 Y. You, X.-X. Zhang, T. C. Berkelbach, M. S. Hybertsen, D. R. Reichman and T. F. Heinz, *Nat Phys*, 2015, **11**, 477-481.

64 Q. Cui, F. Ceballos, N. Kumar and H. Zhao, *ACS Nano*, 2014, **8**, 2970-2976.

65 D. Sun, Y. Rao, G. A. Reider, G. Chen, Y. You, L. Brézin, A. R. Harutyunyan and T. F. Heinz, *Nano Letters*, 2014, **14**, 5625-5629.

66 N. Kumar, Q. Cui, F. Ceballos, D. He, Y. Wang and H. Zhao, *Physical Review B*, 2014, **89**, 125427.

67 X. Yin, Z. Ye, D. A. Chenet, Y. Ye, K. O'Brien, J. C. Hone and X. Zhang, *Science*, 2014, **344**, 488-490.

68 W.-T. Hsu, Z.-A. Zhao, L.-J. Li, C.-H. Chen, M.-H. Chiu, P.-S. Chang, Y.-C. Chou and W.-H. Chang, *ACS Nano*, 2014, **8**, 2951-2958.

69 L. V. Titova, T. B. Hoang, H. E. Jackson, L. M. Smith, J. M. Yarrison-Rice, Y. Kim, H. J. Joyce, H. H. Tan and C. Jagadish, *Appl. Phys. Lett.*, 2006, **89**, 173126.

70 N. Kumar, S. Najmaei, Q. Cui, F. Ceballos, P. M. Ajayan, J. Lou and H. Zhao, *Physical Review B*, 2013, **87**, 161403.

71 L. M. Malard, T. V. Alencar, A. P. M. Barboza, K. F. Mak and A. M. de Paula, *Physical Review B*, 2013, **87**, 201401.

72 Y. Li, Y. Rao, K. F. Mak, Y. You, S. Wang, C. R. Dean and T. F. Heinz, *Nano Letters*, 2013, **13**, 3329-3333.

73 C. Janisch, Y. Wang, D. Ma, N. Mehta, A. L. Elías, N. Perea-López, M. Terrones, V. Crespi and Z. Liu, *Scientific Reports*, 2014, **4**, 5530.

74 O. Lopez-Sanchez, D. Lembke, M. Kayci, A. Radenovic and A. Kis, *Nat Nano*, 2013, **8**, 497-501.

75 H. Yamaguchi, J.-C. Blancon, R. Kappera, S. Lei, S. Najmaei, B. D. Mangum, G. Gupta, P. M. Ajayan, J. Lou, M. Chhowalla, J. J. Crochet and A. D. Mohite, *ACS Nano*, 2015, **9**, 840-849.

76 L. Britnell, R. M. Ribeiro, A. Eckmann, R. Jalil, B. D. Belle, A. Mishchenko, Y.-J. Kim, R. V. Gorbachev, T. Georgiou, S. V. Morozov, A. N. Grigorenko, A. K. Geim, C. Casiraghi, A. H. C. Neto and K. S. Novoselov, *Science*, 2013, **340**, 1311-1314.

77 J. Lu, S. X. Lim and C. H. Sow, *Journal of Materials Science & Technology*, 2015, **31**, 616-629.

78 M. C. Putnam, D. B. Turner-Evans, M. D. Kelzenberg, S. W. Boettcher, N. S. Lewis and H. A. Atwater, *Appl. Phys. Lett.*, 2009, **95**, 163116-163113.

79 Y. Ahn, J. Dunning and J. Park, *Nano Lett.*, 2005, **5**, 1367-1370.

80 R. Graham, C. Miller, E. Oh and D. Yu, *Nano Lett.*, 2010, **11**, 717-722.

81 Y. Gu, J. P. Romankiewicz, J. K. David, J. L. Lensch and L. J. Lauhon, *Nano Lett.*, 2006, **6**, 948-952.

82   J. E. Allen, E. R. Hemesath and L. J. Lauhon, *Nano Lett.*, 2009, **9**, 1903-1908.

83   Y. H. Ahn, A. W. Tsen, B. Kim, Y. W. Park and J. Park, *Nano Lett.*, 2007, **7**, 3320-3323.

84   Y.-J. Doh, K. N. Maher, L. Ouyang, C. L. Yu, H. Park and J. Park, *Nano Lett.*, 2008, **8**, 4552-4556.

85   Z. Yin, H. Li, H. Li, L. Jiang, Y. Shi, Y. Sun, G. Lu, Q. Zhang, X. Chen and H. Zhang, *ACS Nano*, 2012, **6**, 74-80.

86   B. W. H. Baugher, H. O. H. Churchill, Y. Yang and P. Jarillo-Herrero, *Nat Nano*, 2014, **9**, 262-267.

87   D. J. Groenendijk, M. Buscema, G. A. Steele, S. Michaelis de Vasconcellos, R. Bratschitsch, H. S. J. van der Zant and A. Castellanos-Gomez, *Nano Letters*, 2014, **14**, 5846-5852.

88   M. S. Choi, D. Qu, D. Lee, X. Liu, K. Watanabe, T. Taniguchi and W. J. Yoo, *ACS Nano*, 2014, **8**, 9332-9340.

89   J. S. Ross, P. Klement, A. M. Jones, N. J. Ghimire, J. Yan, D. G. Mandrus, T. Taniguchi, K. Watanabe, K. Kitamura, W. Yao, D. H. Cobden and X. Xu, *Nat Nano*, 2014, **9**, 268-272.

90   A. Pospischil, M. M. Furchi and T. Mueller, *Nat Nano*, 2014, **9**, 257-261.

91   H. Zeng, J. Dai, W. Yao, D. Xiao and X. Cui, *Nat Nano*, 2012, **7**, 490-493.

92   X. Xu, W. Yao, D. Xiao and T. F. Heinz, *Nat Phys*, 2014, **10**, 343-350.

93   K. F. Mak, K. L. McGill, J. Park and P. L. McEuen, *Science*, 2014, **344**, 1489-1492.

94   J. Lu, J. H. Lu, H. Liu, B. Liu, L. Gong, E. S. Tok, K. P. Loh and C. H. Sow, *Small*, 2015, **11**, 1792-1800.

95   Y. Shi, J.-K. Huang, L. Jin, Y.-T. Hsu, S. F. Yu, L.-J. Li and H. Y. Yang, *Scientific Reports*, 2013, **3**, 1839.

96   T. S. Sreeprasad, P. Nguyen, N. Kim and V. Berry, *Nano Letters*, 2013, **13**, 4434-4441.

97   W. Han, R. K. Kawakami, M. Gmitra and J. Fabian, *Nat Nano*, 2014, **9**, 794-807.

98   K. F. Mak, K. He, J. Shan and T. F. Heinz, *Nat Nano*, 2012, **7**, 494-498.

99   A. M. Jones, H. Yu, N. J. Ghimire, S. Wu, G. Aivazian, J. S. Ross, B. Zhao, J. Yan, D. G. Mandrus, D. Xiao, W. Yao and X. Xu, *Nat Nano*, 2013, **8**, 634-638.

100   A. Castellanos-Gomez, M. Barkelid, A. M. Goossens, V. E. Calado, H. S. J. van der Zant and G. A. Steele, *Nano Letters*, 2012, **12**, 3187-3192.

101   M. Eginligil, B. Cao, Z. Wang, X. Shen, C. Cong, J. Shang, C. Soci and T. Yu, *Nat Commun*, 2015, **6**.

102   H. Yuan, X. Wang, B. Lian, H. Zhang, X. Fang, B. Shen, G. Xu, Y. Xu, S.-C. Zhang, H. Y. Hwang and Y. Cui, *Nat Nano*, 2014, **9**, 851-857.

103   J. Lu, A. Carvalho, X. K. Chan, H. Liu, B. Liu, E. S. Tok, K. P. Loh, A. H. Castro Neto and C. H. Sow, *Nano Letters*, 2015, **15**, 3524-3532.

104   Y. Liu, H. Nan, X. Wu, W. Pan, W. Wang, J. Bai, W. Zhao, L. Sun, X. Wang and Z. Ni, *ACS Nano*, 2013, **7**, 4202-4209.

105   J. Lu, J. Wu, A. Carvalho, A. Ziletti, H. Liu, J. Tan, Y. Chen, A. H. Castro Neto, B. Özyilmaz and C. H. Sow, *ACS Nano*, 2015, **9**, 10411-10421.

106   L. Cao, S. Yang, W. Gao, Z. Liu, Y. Gong, L. Ma, G. Shi, S. Lei, Y. Zhang, S. Zhang, R. Vajtai and P. M. Ajayan, *Small*, 2013, **9**, 2905-2910.

107   H.-P. Komsa, J. Kotakoski, S. Kurasch, O. Lehtinen, U. Kaiser and A. V. Krasheninnikov, *Physical Review Letters*, 2012, **109**, 035503.

108   H.-J. Kwon, S. Kim, J. Jang and C. P. Grigoropoulos, *Applied Physics Letters*, 2015, **106**, 113111.

109   R. Ulbricht, E. Hendry, J. Shan, T. F. Heinz and M. Bonn, *Reviews of Modern Physics*, 2011, **83**, 543-586.

110   H. Liu, J. Lu, S. H. Tang, C. H. Sow and X. Zhang, *Opt. Lett.*, 2014, **39**, 567-570.

111   L. Li, Y. Yu, G. J. Ye, Q. Ge, X. Ou, H. Wu, D. Feng, X. H. Chen and Y. Zhang, *Nat Nano*, 2014, **9**, 372-377.

112   V. Tran, R. Soklaski, Y. Liang and L. Yang, *Physical Review B*, 2014, **89**, 235319.

113   S. Zhang, Z. Yan, Y. Li, Z. Chen and H. Zeng, *Angewandte Chemie International Edition*, 2015, **54**, 3112-3115.